JOURNAL OF ANATOLIAN PHYSICS AND ASTRONOMY

Anadolu Fizik ve Astronomi Dergisi

2022 Haziran/June Cilt/Volume 02 Sayı/Issue 01

ISSN 2791-8718

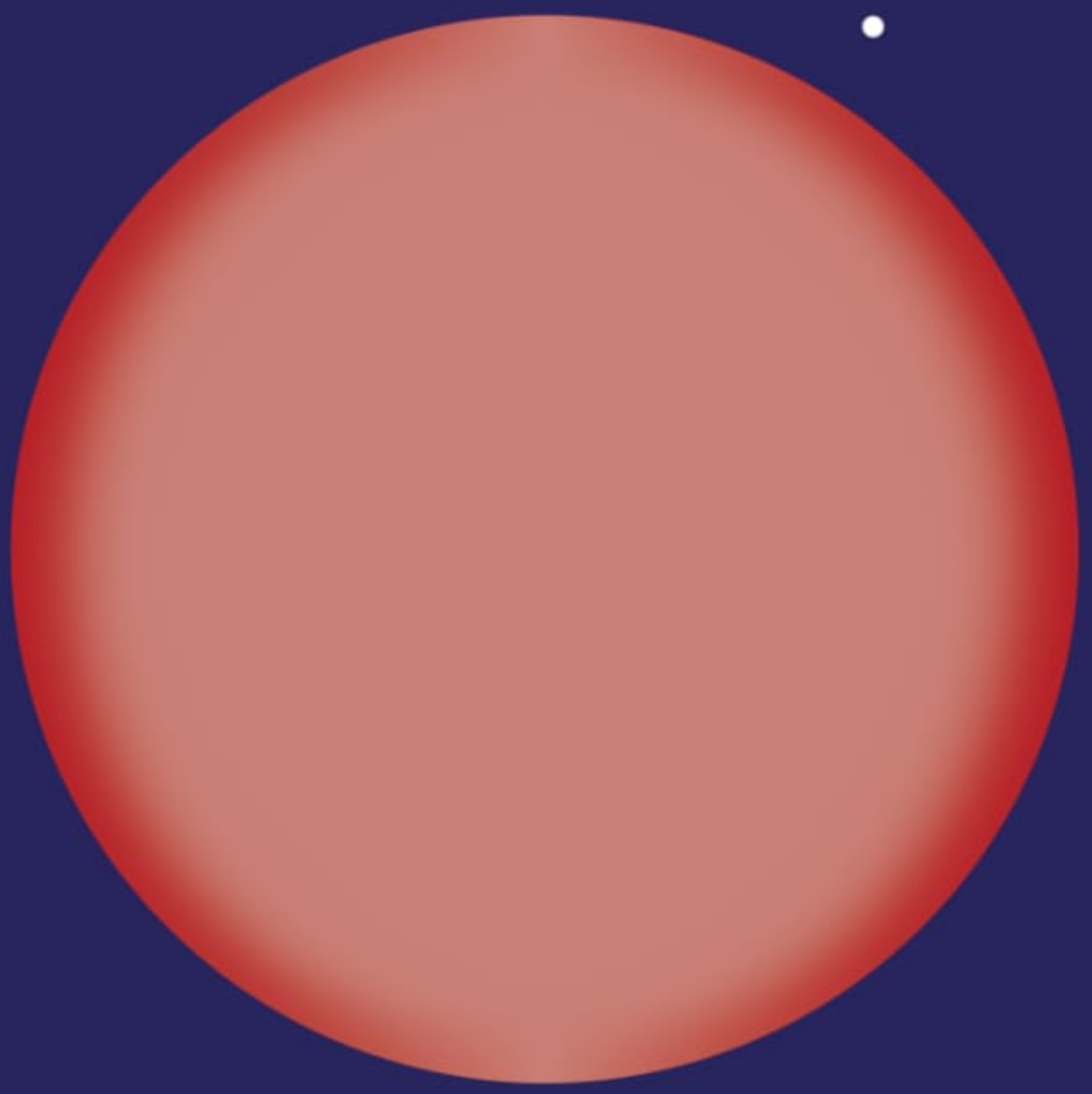

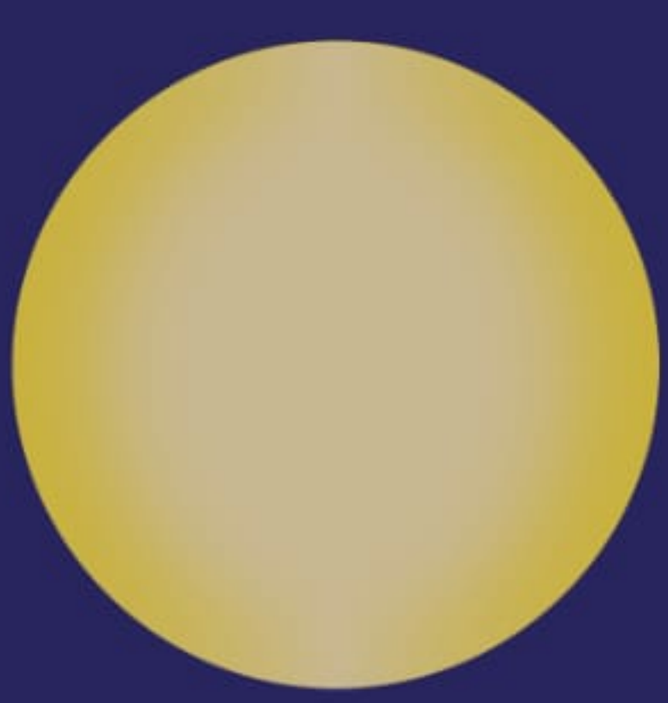

Yayıncı Kuruluş Atatürk Üniversitesi

JAPA

Volume 2 Issue 1 2022

Publisher : Ataturk University

Address : Ataturk University, Faculty of Science, Department of Physics, 25240, Erzurum/Turkey

Phone : +90 442 231 4143

Fax : +90 442 231 4109

E-mail : japa@atauni.edu.tr

ykurucu@atauni.edu.tr

Cover Design: Zafer Lehimler, Assoc. Prof.

Publication date: 30.06.2022

Frequency : 2 issues per year (June, December)

Website : http://bilimseldergiler.atauni.edu.tr/system/physics-astronomy/index

Associate Editors

Physics

Astronomy and Astrophysics

Table of Contents

Atatürk Üniversitesi
Anadolu Fizik ve Astronomi Dergisi
(ISSN: 2791-8718)
Cilt 2, Sayı 1,1-17

Atatürk University
Journal of Anatolian Physics and Astronomy
(ISSN: 2791-8718)
Volume 2, Issue 1,1-17

JAPA

Synthesis of Reduced Graphene Oxide (rGO) Supported Pt Nanoparticles via Supercritical Carbon Dioxide Deposition Technique for PEM Fuel Cell Electrodes

*[1,2] Elif DAŞ and [2,3] Ayşe BAYRAKÇEKEN YURTCAN

[1]Department of Physics, Faculty of Science, Atatürk University, Erzurum, 25240, Turkey
[2]Department of Nanoscience and Nanoengineering, Graduate School of Natural and Applied Science, Atatürk University, Erzurum 25240, Turkey
[3]Department of Chemical Engineering, Faculty of Engineering, Atatürk University, Erzurum 25240, Turkey

ORCID*[1]:https://orcid.org/0000-0002-3149-6016

Research Type: Research Article
Received: 15.03.2022, Accepted: 03.04.2022
*Corresponding author: das.elif@gmail.com (E.Daş)

Abstract

In this work, the preparation of reduced graphene oxide (rGO) supported Pt nanoparticles by using the supercritical carbon dioxide ($scCO_2$) deposition technique is investigated. For this purpose, firstly, graphite oxide synthesis was made similar to the literature reports and then two different reducing agents (DMF and hydrazine hydrate) were used to prepare rGO support materials, called as rGO1 and rGO2, respectively. Finally, Pt nanoparticles (NPs) were formed on the rGO support materials. The effect of the reducing agent type and also of the catalyst preparation technique on the fuel cell performance were examined with spectroscopic, microscopic, and electrochemical techniques. From the results obtained, it appears that the properties of rGO vary significantly depending on the reducing agent used. Moreover, the electrode containing Pt/rGO1 has exhibited better cell performance compared to the Pt/rGO2.
Key Words: PEM fuel cell electrodes, Pt nanoparticles, support material, reducing agent.

PEM Yakıt Pili Elektrotları için Süperkritik Karbondioksit Depozisyon Tekniği ile İndirgenmiş Grafen Oksit (rGO) Destekli Pt Nanoparçacıklarının Sentezi

Özet

Bu çalışmada, süperkritik karbondioksit depozisyon tekniği ($scCO_2$) kullanılarak indirgenmiş grafen oksit destekli (rGO) Pt nanoparçacıklarının sentezi araştırılmaktadır. Bu amaçla, öncelikle, literatüre benzer olarak grafit oksit sentezi gerçekleştirildi ve daha sonra iki farklı indirgeyici ajan (DMF ve hidrazin hidrat) ile sırasıyla rGO1 ve rGO2 olarak isimlendirilen rGO destek malzemeleri hazırlandı. Son olarakta, Pt nanoparçacıkları (NPs) rGO destek malzemeleri üzerine oluşturuldu. Indirgeyici ajan türünün ve katalizör hazırlama tekniğinin yakıt pili performansı üzerindeki etkisi spektroskopik, mikroskopik ve elektrokimyasal tekniklerle incelendi. Elde edilen sonuçlardan, kullanılan indirgeyici ajana bağlı olarak rGO malzemesinin özelliklerinin önemli ölçüde değiştiği görülmektedir. Ayrıca, Pt/rGO1 içeren elektrot, Pt/rGO2'ye kıyasla daha iyi pil performansı sergilemiştir.

Anahtar Kelimeler: PEM yakıt pili elektrotları, Pt nanoparçacıkları, destek malzemesi, indirgeyici ajan.

1. Introduction

Fuel cells are one of the important clean energy converting devices. Polymer electrolyte membrane fuel cells (PEMFCs) are the most studied among all types of fuel cells, especially for stationary, portable and automotive applications. It is mainly because of their high energy conversion efficiency, high energy density, low operation temperature, fast start-up and response times and low emission [1-4]. However, there are some critical obstacles preventing the commercialization and common usage of PEM fuel cells, such as high cost of platinum (Pt) catalysts and low durability of the catalyst layer [5-9]. For this reason, many strategies have been developed to increase catalytic activity and to reduce the usage of Pt-based catalysts. One of these strategies is to use carbon-based material as catalyst support [10-13]. Because support material not only provides conductivity but also provides a high surface area to improve the Pt utilization efficiency. Up to now, many alternative carbon-based materials such as carbon nanotubes, carbon aerogels, mesoporous carbon, fullerene, graphitic and carbon fibers have been tried as support materials [3, 14-20]. But, none of these prevalently used support materials can exactly fulfill the essential requirements. Hence, efforts must be put in for the development of new catalyst support.

In the past several years, graphene, with unrivalled 2D structure and properties including high conductivity, high specific surface area, high tensile strength, and etc., has been regarded as an alternative catalyst support for Pt nanoparticles (NPs) due to these superior features, have been commonly studied [21-26]. In literature, numerous methods have been developed to prepare graphene, including mechanical exfoliation of graphite (scotch-tape method), epitaxial growth, chemical vapor deposition, liquid phase exfoliation of graphite, chemical reduction of GO [27, 28]. Among all these methods, the chemical reduction of GO is the most promising method for mass production of graphene and this method involves of oxidation/reduction steps [29, 30]. Typically, graphite material is converted to GO via strongly oxidizing agents such as HNO_3, H_2SO_4, H_3PO_4, $KMnO_4$ and this oxidation step results in the widening of intersheet spacing of carbon layers due to the emplacement of functional groups onto the layer [31]. Following oxidation step, GO becomes hydrophilic in nature due to the polar oxygen functional groups and as a result, GO is easily dispersible in various solvents, especially in water [30]. The Van der Waals forces weaken because oxygen groups are

introduced in GO structure which results in a partial degradation of the sp^2 lattice into a sp^2-sp^3 sheet with less π-π stacking ability. These changes make GO non-conductive as it lacks the conducting graphitic network. The conducting property of GO can be recovered by the reduction process, such as chemical reduction (e.g. via reducing agents) and thermal reduction (e.g. via annealing at high temperature under inert gas), which eliminates functional groups. The efficiency of the reduction process can be measured with O/C ratio and this ratio decreases significantly after reduction process. Also, according to the literature reports, in the high electrical conductivity required applications, it is necessary to reduce the O/C ratio below 1% [2]. However, in some cases, partially reduction also is desired, because the surface functional groups on the material serve as the anchoring sides for metal NPs while preventing restacking and aggregation to graphite form during the chemical reduction to graphene. Therefore, many studies are conducted in the literature on the preparation of Pt NPs onto the graphene-based materials such as graphene nanoplatelets (GNPs), graphene nanosheets, rGO, and functionalized graphene (g-GO) [2, 24, 32-34].

Along with the catalyst support material used, the catalyst preparation technique is also momentous and among the proposed catalyst preparation techniques in the literature, $scCO_2$ deposition technique has attracted attention in last years, due to its important advantages [8, 35-37]. This technique employs the dissolution of a metal precursor in the $scCO_2$ environment leading to the adsorption of the precursor into the support. Later, the metal precursor is converted to the corresponding metal via ex-situ or in-situ ways [38]. Thereby, supported metal NPs are obtained.

In most of the earlier reports on the Pt/rGO catalysts, on one hand, Pt NPs were formed on support during the reduction process of graphite oxide (GO), on the other hand, common techniques were used to create Pt NPs on the support. In our work, firstly, production of rGO support materials were achieved by using two different reducing agents and then Pt NPs were employed over these supports materials by using $scCO_2$ deposition technique. As far as we know, the decoration of Pt NPs on rGO support materials with the help of this technique and their fuel cell performances is presented in the literature for the first time. So, we believe that our study will make important contributions to the literature.

2. Material and Methods

2.1. Materials

STREM brand 1,5-dimethyl platinum cyclooctadiene ($PtCODMe_2$) was purchased for using as Pt organometallic precursor. Natural graphite flakes (average particle size 325 mesh) were procured from Alfa Aesar and used as recieved. Potassium peroxodisulfate ($K_2S_2O_8$ ≥99.9%), phosphorous pentoxide (P_2O_5, ≥98%), sulfuric acid (H_2SO_4 98%), sodium nitrate ($NaNO_3$ ≥99.9%), potassium permanganate ($KMnO_4$ ≥99.9%), hydrogen peroxide (H_2O_2, 30%) were purchased from Sigma–Aldrich for use in GO synthesis and same brand dimethylformamide (DMF) and hydrazine hydrate were used as GO reducing agents. All chemicals were used without any further treatment. Also, high purity CO_2, N_2, O_2, H_2 gases were purchased from Habaş.

2.2. Preparation of Graphite Oxide (GO), Reduced Graphene Oxide (rGO) Materials

Firstly, GO synthesis was made from natural graphite powder by using improved synthesis proposed by Kovtyukhova et al. [39]. Subsequently, the GO was reduced with two different reducing agents (DMF and hydrazine hydrate) to obtain rGO materials. The details of the rGO synthesis procedure via DMF is descibed in our earlier report [40] and the resulting product was called as rGO1 in this study.

On the other hand, hydrazine hydrate material was also used as a reducing agent to the synthesis of rGO. Briefly, 0.5 g of dried GO was thoroughly dissolved in 0.5 L of water with the help of an ultrasonic bath until there was no visible particle in the solution. Subsequently, 5 mL of reducing agent was added into the solution and the reflux system was connected for the reduction process. The solution refluxed for 18 h at 100 ºC. When the reflux process was completed, floating black particles were observed on the solution, which is due to the reduction of GO. Lastly, the solution was cooled down to room temperature, filtered and washed several times with water and methanol, respectively. After evaporation of the solvents with the rotary evaporator, the final product was obtained was called as rGO2.

2.3. Synthesis of rGO Supported Pt NPs

Pt NPs were created on the rGO support materials by using $scCO_2$ deposition method in a high pressure vessel. The details of synthesis procedure were mentioned in our previous studies [37, 41, 42]. To eliminate similarity, the schematic view of the experimental setup was shown in Fig. 1.

2.4. Characterization of the Materials

2.4.1. Characterization of physical properties

The surface structure parameters of the support materials were analyzed with BET isotherms by using the Micromeritics 3Flex analyzer. The samples were degassed at 90 ˚C for 12 h before taking measurements. Thermogravimetric (TG) analysis was performed using a Netzsch thermal analyzer with the heating rate of 10 ºC/min and the flow rate of 30 mL/min in aluminum crucibles under air atmosphere. The Raman spectra of the pristine graphite, rGO1 and rGO2 materials were measured by using a WITech alpha 300R Raman system. Surface morphology and chemical composition of the support materials were observed by Zeiss Sigma 300 model scanning electron microscope (SEM), which is equipped with energy-dispersive X-ray spectroscopy (EDS). The homogeneity of the Pt NPs on the support materials were analyzed through the JEOL 2100 JEM transmission electron microscopy (TEM). TEM samples were prepared by dispersing supports and catalyst materials in ethanol to form a homogeneous suspension. Then, the suspension was dropped on copper grid for observation.

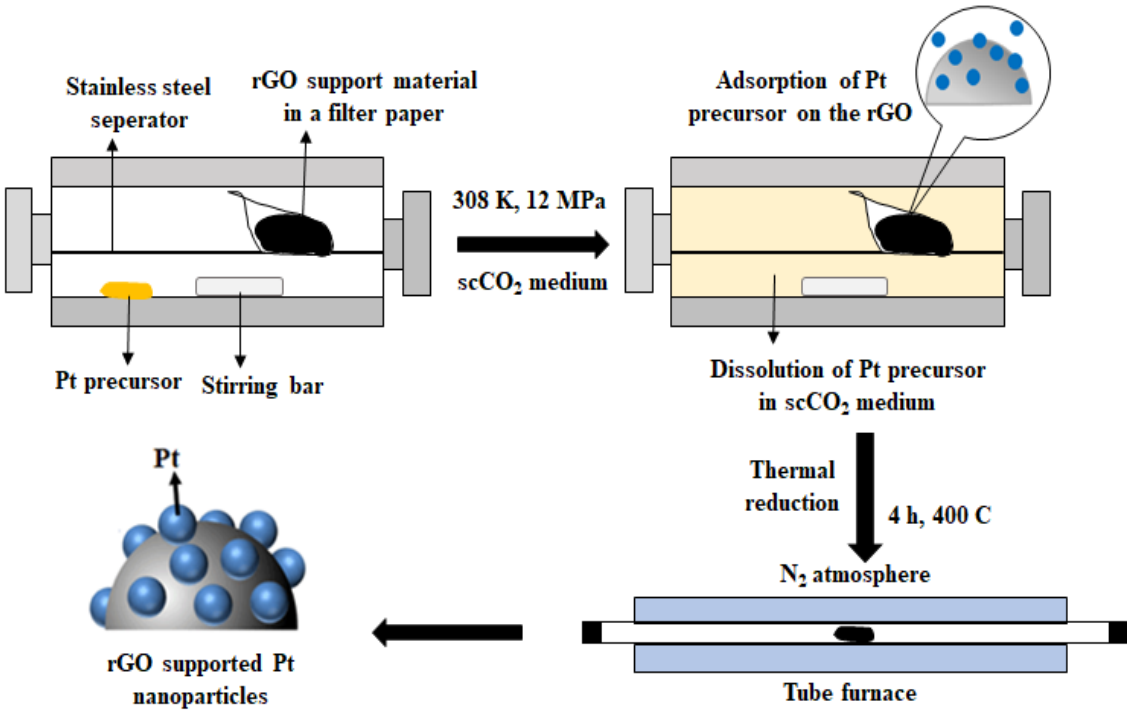

Figure 1. Experimental setup used for the decoration of Pt NPs on rGO support materials

2.4.2. Characterization of electrochemical properties

The ex-situ electrochemical studies of the support materials were performed in a standard three-electrode cell, using a VersaStat potentiostat/galvanostat. A silver-silver chloride electrode (Ag/AgCl, Cl^-) with 3.5 M KCI solution as a reference electrode, a Pt wire as a counter electrode and glass carbon (GC) as working electrode were employed. The obtained cycling voltammograms were converted and presented in terms of normal hydrogen electrode (NHE). To prepare working electrode catalyst ink, the required amount of the support material, deionized water, 1,2-propanediol and 15% Nafion solution were mixed till obtaining uniform ink. Then, the ink was dropped on the GC with a micropipette and left to dry at the room environment. The amount of the material on the GC was maintained as 22 μg/cm^2 for each electrode.

Cyclic voltammetry (CV) measurements for hydrogen oxidation reactions (HOR) were carried out in a N_2 saturated 1 M H_2SO_4 electrolyte (potential range: 0-1.2V, scan rate: 50 mV/s). Then, in order to apply electrochemical oxidation, the electrode was subjected to a constant potential of 1.2 V for 24 h. At the end of 24 h, the same test procedure was repeated. Thus, the oxidation characteristics of the rGO1 and rGO2 materials were evaluated before and after the electrochemical oxidation treatment. The tests were repeated several times for both support materials until the same results were obtained.

2.5. Fabrication of Membrane Electrode Assembly (MEA) and Fuel Cell Tests

The in-situ electrochemical tests were performed in a single fuel cell system (Henatech™). Firstly, cathode and anode electrodes were prepared. The details related to electrode preparation by using the spraying method can be found in our previous papers [4, 9]. The Pt loading was set to 0.4 mgPt/cm^2 for all catalyst layers. Then, prepared electrodes were hot pressed at 130 ºC and 400 psi for 3 min on to the Nafion 212 membrane to obtain MEA which has 4.41 cm^2 active surface area. Finally, the catalytic activities of MEAs were tested in a commercial PEM fuel cell test station. Hydrogen gas was fed from the anode side and oxygen gas fed from the cathode side, respectively. However, before the delivery of hydrogen and oxygen to the system, the cell was purged with nitrogen gas for a while. Meanwhile, the temperature of the cell and humidifier columns were adjusted to 70 °C. Subsequent to the purging, reactant gases were sent to the system. Then, polarization curves were taken by sweeping the voltage between OCV and 0.1V. In these measurements, the cell was equilibrated for at least 1 min at each point.

3. Results and Discussion

In heterogeneous catalysts, the vast majority of reactions take place on the catalyst surface. Therefore, it is very essential to accurately determine the surface area of the catalyst support. Likewise, the porosity and surface area knowledge of different support materials are of great importance in understanding their structure, formation, and potential applications. Surface area measurements are mainly carried out by the method of Brunauer, Emmett, and Teller (BET) [43]. According to this method, when a solid surface is reacted with a gas, the gas molecules attach to the surface and form adsorbed layers. The amount of adsorption is proportional to the total surface area of the sample. To determine the textural and structural properties of prepared support materials (rGO1 and rGO2), BET analysis was performed. The detailed BET results of rGO1 support material were given in our previous paper [40]. Hence, Fig. 2 shows the N_2 adsorption/desorption isotherms of the rGO2 support material and the corresponding pore size distribution. The isotherm of the rGO2 support material can be identified as type IV according to the International Union of Pure and Applied Chemistry (IUPAC) classification. Type IV isotherms are characteristic of materials containing mesopores and it shows a hysteresis loop from P/P_o=0.5 to P/P_o=1.0 which is H3 type hysteresis according to the IUPAC classification. This is attributed to the characteristic of aggregates of plate-like particles giving rise to slit-shaped pores and is common for carbon-like samples [44, 45].

According to the obtained BET results (Table 1), the surface area of the pristine graphite with a layered structure was found to be 13.7 m^2/g [40]. After the chemical oxidation process, it was observed that the material structure changed and a decrease in the surface area (3.3 m^2/g) occurred. Furthermore, after the reduction of GO with two different reducing agents, it was observed that the surface area values and pore volume values increased. However, the obtained surface area values were lower than the theoretical value (2630 m^2/g) of single graphene sheet. This is attributed to the restacking phenomenon of the graphene sheets owing to strong van der Waals forces.

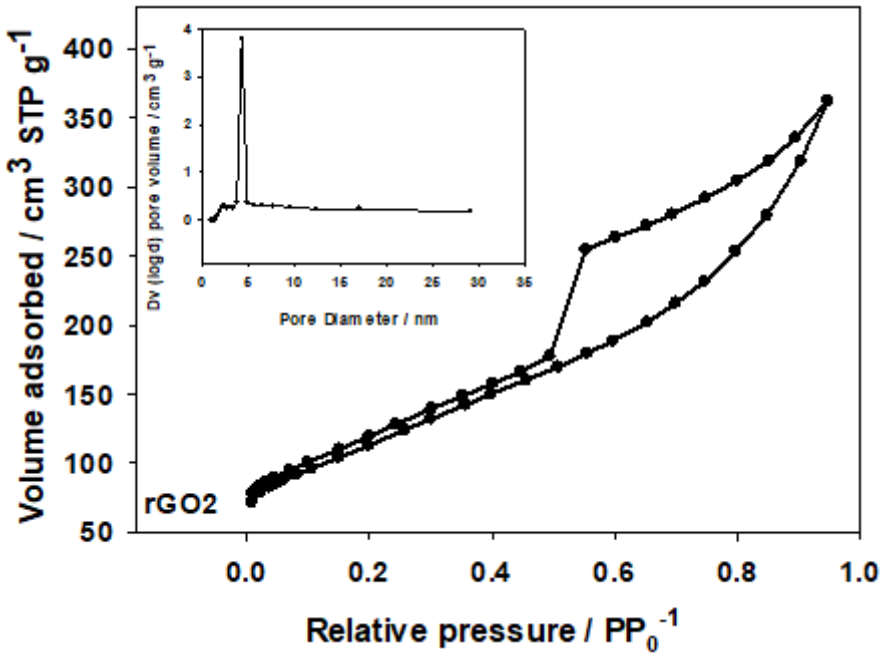

Figure 2. BET-N_2 adsorption/desorption isotherm and pore size distribution of the rGO2 support material

Table 1. Surface areas, pore volumes and pore sizes of the materials

Support	Total Surface Area (m^2/g)	BJH Pore Volume (cc/g)	BJH Average Pore Size (Å Diameter))	Ref.
Graphite	13.7	0.0270	22.4	[40]
GO	3.3	0.0095	31.3	[40]
rGO1	41.0	0.0513	22.5	[40]
rGO2	484.0	0.5050	22.2	(this study)

The thermal stabilities of the support materials were analyzed by TGA as shown in Fig. 3 (a). All measurements were carried out in air atmosphere up to 1000 ºC. In both support materials, the initial weight loss was observed between 250-500 °C and this loss can be attributed to the gasification of the carbonaceous material due to oxidation of rGO [40]. Above 500 ºC, almost a constant weight was observed up to 1000 ºC and both support materials showed very similar trend in weight loss by temperature. Also, the Pt loading amount of the catalysts were calculated from the weight percent loss difference between rGO supports and the Pt/rGO catalysts (Fig. 3 (b-c)). The calculated Pt loading (wt.%) values were given in Table 2 and it was observed that the Pt loading on rGO1 support was 25.2%, while the loading on rGO2 support was 20%.

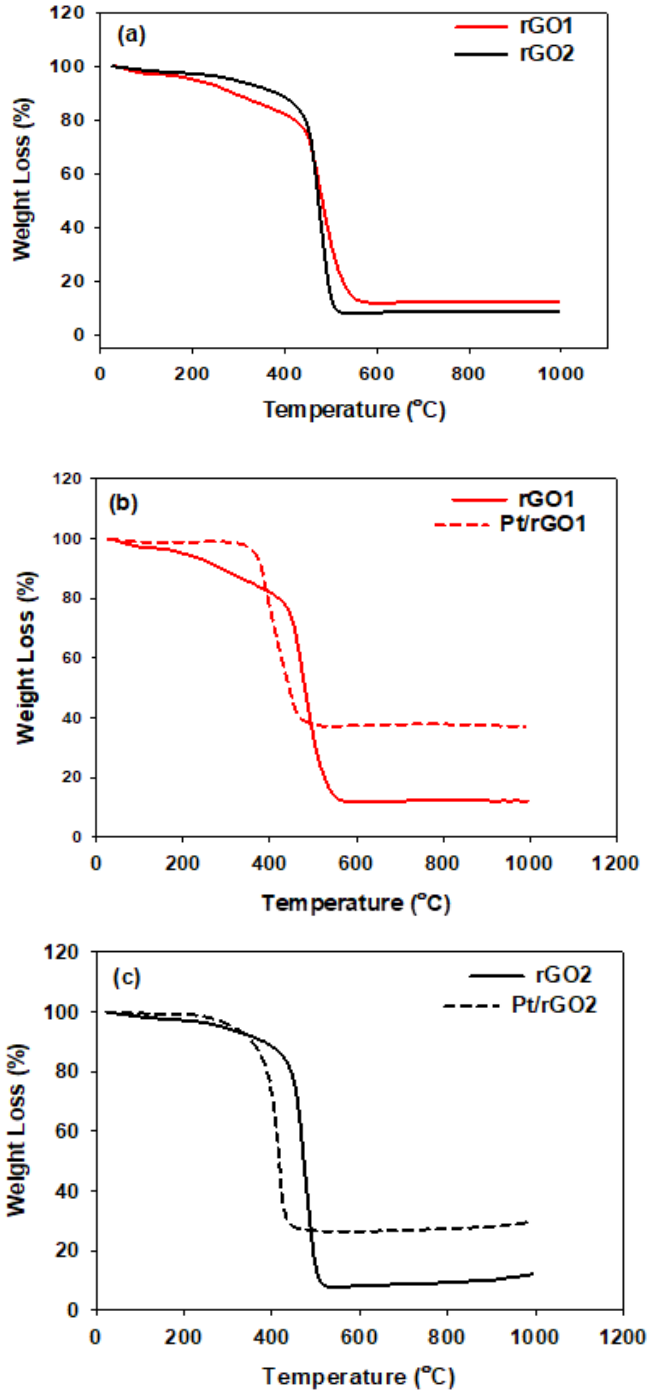

Figure 3. TGA curves of synthesized supports and catalysts

Table 2. Pt loading amounts of the catalysts

Catalyst	Pt [wt.%]
Pt/rGO1	25.2
Pt/rGO2	20

The morphology of the prepared support materials was investigated by using SEM. The obtained SEM plan-view images and corresponding EDS spectras were given in Fig. 4. The starting material was flake graphite having a flat morphology as shown in Fig. 4 (a). After the chemical oxidation process of graphite, the smooth flat structure turned into a rough and porous structure (Fig. 4 (b)). Also, the oxygen content increased owing to the formation of the oxygen functional groups on the edges and the basal planes of the rGO structure. In addition to the C and O atoms, the presence of new atoms such as S, K, Mn, Na were observed in the structure. Subsequently, the reduction process was carried out by using two different chemical reduction routes (as decribed in experimental part). Fig. 4 (c-d) shows the SEM images and corresponding EDS spectrums of the obtained rGO materials. As seen in the Fig. 4 (c), the rough surface structure of the GO changed into more uniform structure after reduction by DMF at reflux condition. Also, the purity of the material was checked by means of EDS and the spectra revealed that the structure still contain some residual impurities. In Fig. 4 (d) case, hydrazine hydrate was used to reduce GO. The obtained images showed that the structure contains micron-sized well-dispersed wrinkle flakes.

Fig. 5 displays TEM images of the rGO support materials and catalysts under different magnifications. In Fig. 5 (a) image, the rGO1 support material resembles a transparent ultrathin structure comprising few thin ripples within the plane, which is remarkably different from the opaque and smooth resemblance of pristine graphite flakes. This transparency and rippled characteristic of material, suggests that the material consists of a few thin layer or monolayer. Due to the wrinkled and overlapped structure, the individual graphene sheets can effectively link together and serve as great electrical conductor, resulting in high electrical conductivity [46]. On the other hand, the TEM image (Fig. 5 (b)) of rGO2 support material is composed of micrometer-sized wrinkled flakes with a high-transparency chiffon like texture. This wrinkle feature of the material prevents the aggregation of the dried sample due to van der Waals forces and play an important role in increasing the surface area [47].

Additionally, the TEM images of rGO supported Pt catalysts were also taken and results were given in Fig. 5 (c-d). It was clearly observed that the Pt NPs with spherical shaped particles were dispersed homogeneously on the rGO support materials. These results suggested that the $scCO_2$ deposition technique is a very accomplished method on the preparation of Pt NPs on rGO support materials.

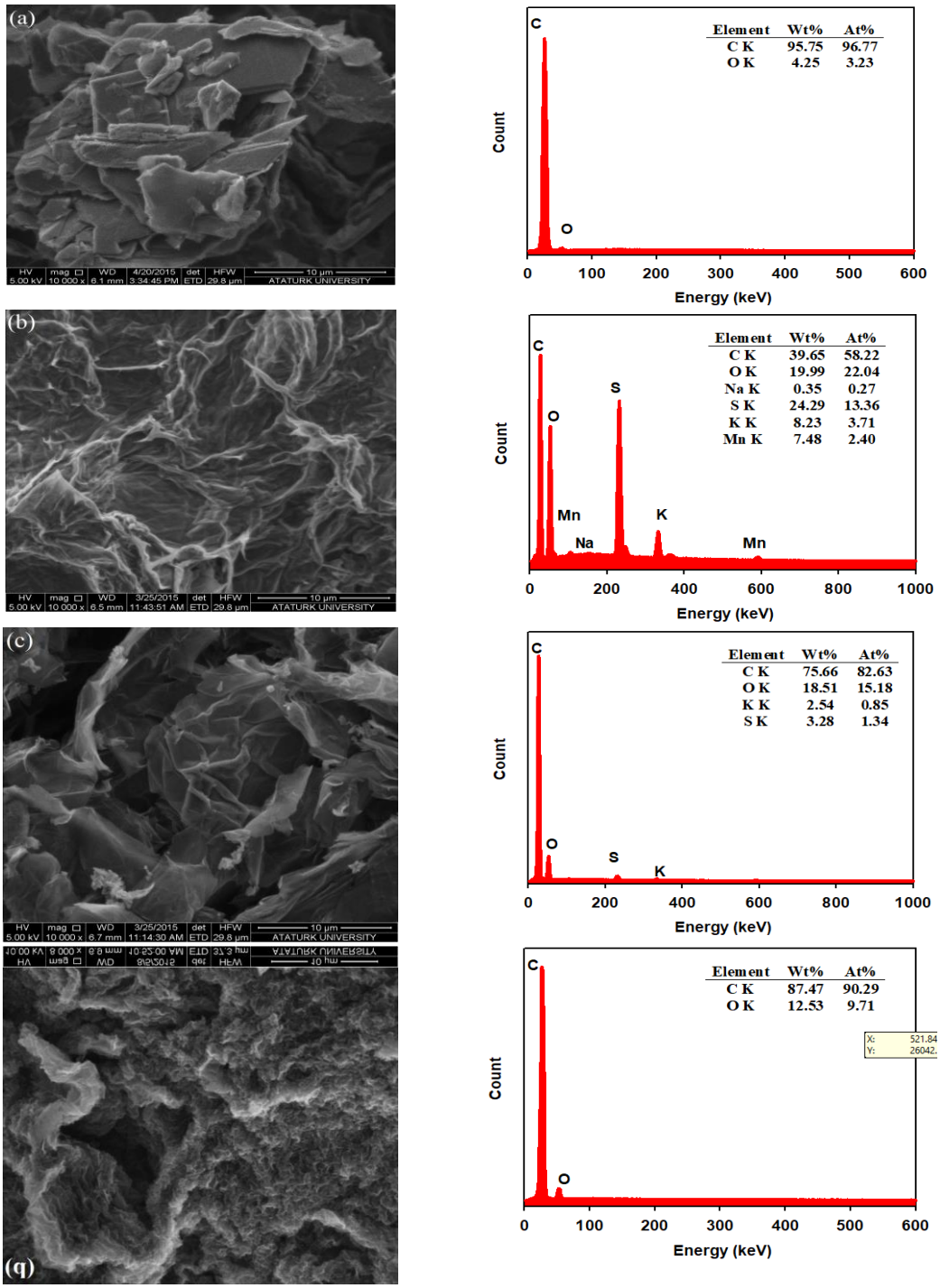

Figure 4. SEM and EDS results of (a) pristine graphite (b) GO (c) rGO1 (d) rGO2

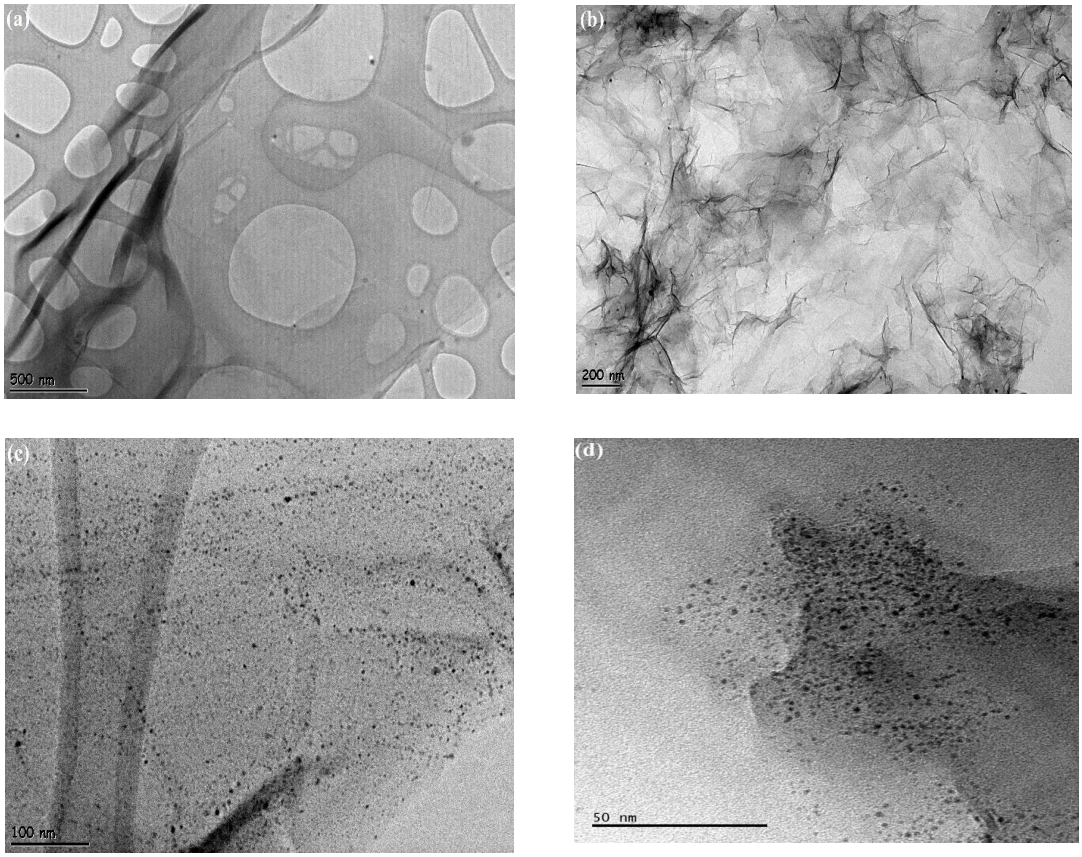

Figure 5. TEM images of (a) rGO1 (b) rGO2 (c) Pt/rGO1 (d) Pt/rGO2

Raman spectroscopy is an important characterization method used to evaluate the reduction effect and the main vibration peaks of carbon-based materials. Therefore, the pristine graphite and rGO support materials were characterized by Raman spectroscopy, as shown in Fig. 6. Two main characteristic peaks were observed for all the samples as D and G band. These bands are attributed to the defect/disorder states and the sp^2-bonded in plane vibration of carbon atoms, respectively [29, 48]. For the pristine graphite, the D and G band positions are centered at 1346 and 1572 cm^{-1} respectively, while for rGO1 and rGO2, these bands are centered at 1352 and 1593 and at 1352 and 1591 cm^{-1} respectively. The band positions and intensity ratios (I_D/I_G) of materials are summarized in Table 3.

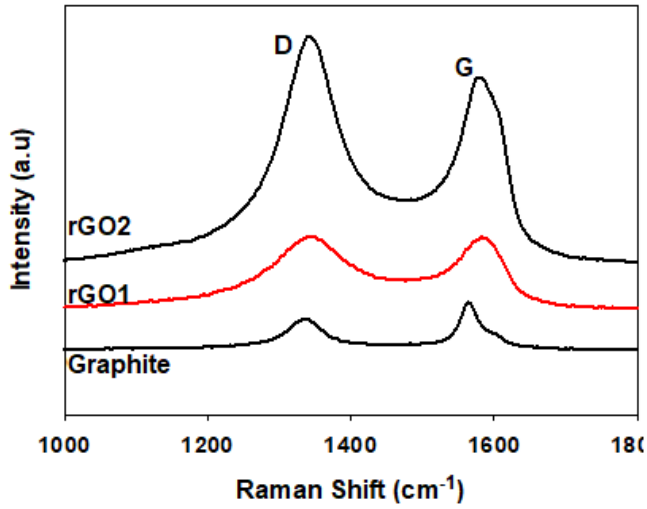

Figure 6. Raman spectra of pristine graphite, rGO1 and rGO2 support materials

Table 3. Analyses of Raman spectra

Sample	D band (cm^{-1})	G band (cm^{-1})	I_D/I_G
Graphite	1346	1572	0.48
rGO1	1352	1593	0.88
rGO2	1352	1591	1.22

As shown on Fig. 6 and Table 3, the Raman peaks showed change in band shape and band position. In the case of rGO, it is appears that the D band position of both rGO material is almost unchanged. However, the G band position of rGO's exhibit a shift toward higher wavenumber compare to the pristine graphite, which attributes to the restoration of the sp^2 bond of the carbon structure.

The intensity ratio (I_D/I_G) of these bands provides important information about the level of the disorder. The I_D/I_G ratio of graphite, rGO1 and rGO2 materials was found to be 0.48, 0.88 and 1.22 respectively. The high intensity ratio reveals that the defects increase after the reduced process. This increase of I_D/I_G upon GO reduction is normal and could be attributed to the generation of edge atoms in the structure and also residual oxygen containing groups, vacancies and topological defects from degraded functional groups.

On the other hand, a number of activity losses are observed in the catalyst and catalyst support materials under harsh operating conditions of PEM fuel cells. These losses are usually caused by reason such as fuel starvation, poor water management, CO poisoning in the anode electrode. If the fuel in the anode is insufficient, the voltage rises up to the value needed to oxidize the water to maintain the current. However, such a high potential leads to carbon corrosion and metal dissolution, causing the anode catalyst layer to degrade. Therefore, the use of corrosion-resistant materials is of great importance. For this purpose, the cyclic voltammetry measurements were carried out to examine the electrochemical oxidation (carbon corrosion) of rGO materials. The obtained voltammograms were shown in Fig. 7. The electrochemical oxidation tests were performed by applying 1.2 V in both support materials for 24 h. The voltammograms were performed in the range of -0.1 to 1.1 V against the normal hydrogen electrode (NHE). In both support

materials, faradaic peaks were observed at around 0.6 V of anodic scan and around 0.55 V of cathodic scan, corresponding to redox reactions of surface functionalities which provide pseudocapacitance. However, these anodic and cathodic peaks become more pronounced after the electrochemical oxidation. Furthermore, the peaks are shifted to higher and lower values after the electrochemical oxidation. Similar findings were observed for many carbon-based support materials which is reported in the literature [12, 49, 50] and ascribed to the dependence on the surface concentration of hydroquinone/quinone redox couple [51]. Also, it was seen that the CV currents have increased after reduction process for both support materials, which reflect surface area changes as well as the formation of new surface oxide groups, is correlated with the extent of carbon corrosion [50], although the exact relationship is not clear. According to the obtained CV results, it can be said that the rGO1 exhibits better electrochemical properties compared to rGO2 support.

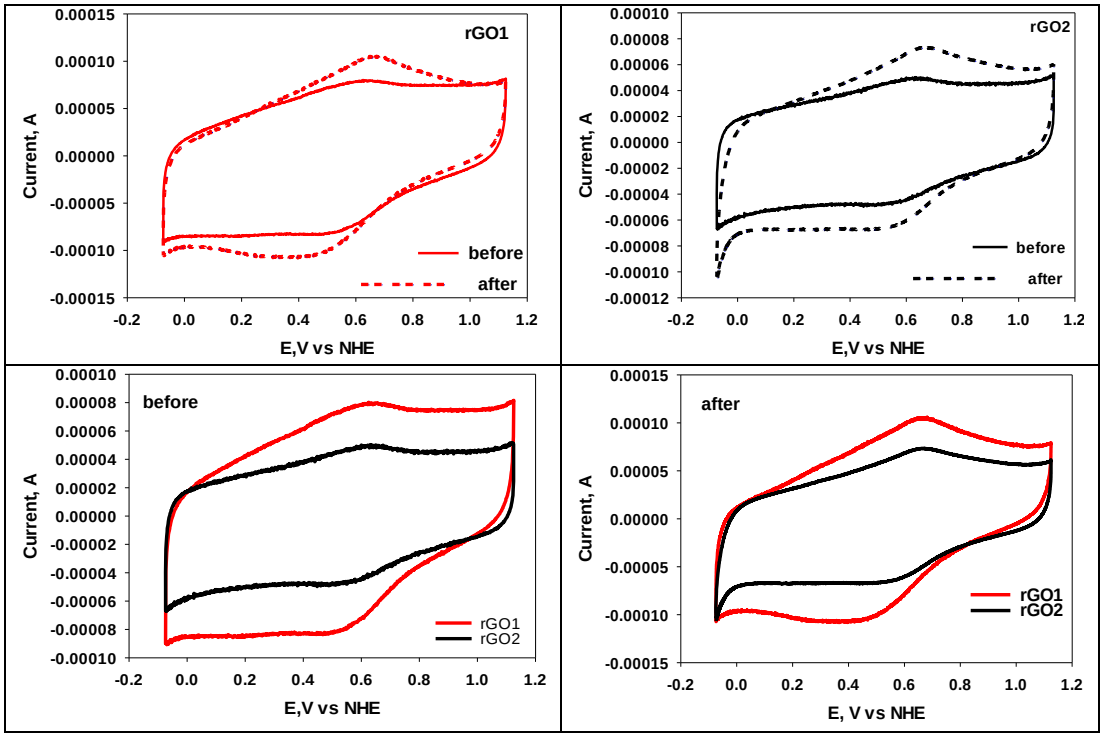

Figure 7. Cyclic voltammograms for rGO1 and rGO2 support materials before and after electrochemical oxidation

Fuel cell performances were also evaluated by using a single cell test station and the obtained polarization curves were given in Fig. 8. It was observed that the performance of the catalyst prepared with rGO1 support is higher than that of the rGO2 supported catalyst, especially at high current density region. This high fuel cell performance can be attributed to the structural properties of rGO1 support material, which provides superior mass transfer capability for reaction species compared to the rGO2 support material. The maximum power density achieved with the Pt/rGO1 catalyst is approximately 635 mW/cm^2 and higher than those reported maximum power density values for Pt/rGO (320 mW/cm^2) [52], Pt/rGO (375 mW/cm^2) [2], the partially GO-Pt (161 mW/cm^2) [25].

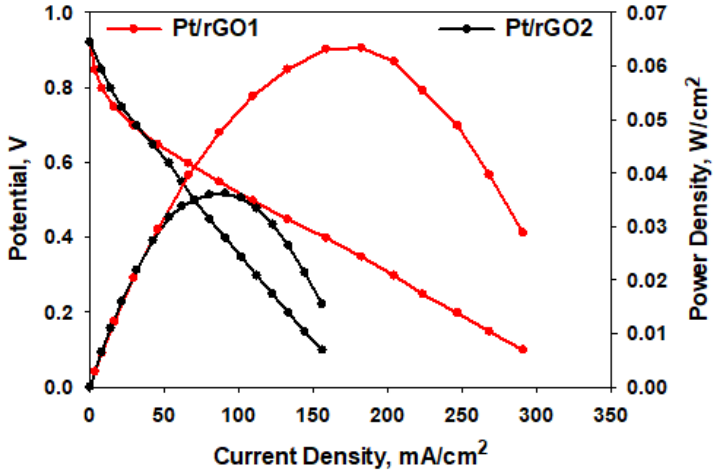

Figure 8. PEM fuel cell polarization curves

4. Conclusion

In summary, we have demostrated a facile and effective method for the preparation of rGO supported Pt NPs catalysts. Firstly, synthesis of rGO support materials were achieved by using two different reducing agents and then Pt NPs were created over these support materials by using $scCO_2$ deposition technique. To the best our knowledge, this is the first example of rGO supported Pt NPs where Pt NPs were decorated on the support by using $scCO_2$ deposition technique. The physicochemical and electrochemical experimental results showed that reducing agents used in the rGO support materials significantly affect the properties of the support materials and also PEM fuel cell performances. The maximum power density of 635 $mWcm^{-1}$ was achieved with Pt/rGO1 catalysts.

Acknowledgments
This work was supported by Atatürk University Scientific Research Project Council (Project No: 2014/79).

Conflicts of interest
The authors declare that there are no potential conflicts of interest relevant to this article.

References

[1] Acres G. J. K. Recent advances in fuel cell technology and its applications. Journal of Power Sources. 2001;100:60-66.

[2] Ozdemir OK. A novel method to produce few layers of graphene as support materials for platinum catalyst. Chemical Papers. 2018;73:387-95.

[3] Kou R, Shao Y, Wang D, Engelhard MH, Kwak JH, Wang J, et al. Enhanced activity and stability of Pt catalysts on functionalized graphene sheets for electrocatalytic oxygen reduction. Electrochemistry Communications. 2009;11:954-7.

[4] Daş E, Yurtcan AB. Effect of carbon ratio in the polypyrrole/carbon composite catalyst support on PEM fuel cell performance. International Journal of Hydrogen Energy. 2016;41:13171-9.

[5] Zhang M, Xie J, Sun Q, Yan Z, Chen M, Jing J. Enhanced electrocatalytic activity of high Pt-loadings on surface functionalized graphene nanosheets for methanol oxidation. International Journal of Hydrogen Energy. 2013;38:16402-9.

[6] Shao Y, Zhang S, Wang C, Nie Z, Liu J, Wang Y, et al. Highly durable graphene nanoplatelets supported Pt nanocatalysts for oxygen reduction. Journal of Power Sources. 2010;195:4600-5.

[7] Hellman H, Vandenhoed R. Characterising fuel cell technology: Challenges of the commercialisation process. International Journal of Hydrogen Energy. 2007;32:305-15.

[8] Bayrakçeken A, Smirnova A, Kitkamthorn U, Aindow M, Türker L, Eroğlu İ, et al. Pt-based electrocatalysts for polymer electrolyte membrane fuel cells prepared by supercritical deposition technique. Journal of Power Sources. 2008;179:532-40.

[9] Daş E, Bayrakçeken Yurtcan A. PEDOT/C Composites used as a Proton Exchange Membrane Fuel Cell Catalyst Support: Role of Carbon Amount. Energy Technology. 2017;5:1552-60.

[10] Dicks AL. The role of carbon in fuel cells. Journal of Power Sources. 2006;156:128-41.

[11] Oh H-S, Lee J-H, Kim H. Electrochemical carbon corrosion in high temperature proton exchange membrane fuel cells. International Journal of Hydrogen Energy. 2012;37:10844-9.

[12] Wang J, Yin G, Shao Y, Zhang S, Wang Z, Gao Y. Effect of carbon black support corrosion on the durability of Pt/C catalyst. Journal of Power Sources. 2007;171:331-9.

[13] Yu X, Ye S. Recent advances in activity and durability enhancement of Pt/C catalytic cathode in PEMFC. Journal of Power Sources. 2007;172:145-54.

[14] Liu B, Creager S. Carbon xerogels as Pt catalyst supports for polymer electrolyte membrane fuel-cell applications. Journal of Power Sources. 2010;195:1812-20.

[15] Cheng K, He D, Peng T, Lv H, Pan M, Mu S. Porous graphene supported Pt catalysts for proton exchange membrane fuel cells. Electrochimica Acta. 2014;132:356-63.

[16] Arbizzani C, Righi S, Soavi F, Mastragostino M. Graphene and carbon nanotube structures supported on mesoporous xerogel carbon as catalysts for oxygen reduction reaction in proton-exchange-membrane fuel cells. International Journal of Hydrogen Energy. 2011;36:5038-46.

[17] Sebastián D, Calderón JC, González-Expósito JA, Pastor E, Martínez-Huerta MV, Suelves I, et al. Influence of carbon nanofiber properties as electrocatalyst support on the electrochemical performance for PEM fuel cells. International Journal of Hydrogen Energy. 2010;35:9934-42.

[18] Trogadas P, Fuller TF, Strasser P. Carbon as catalyst and support for electrochemical energy conversion. Carbon. 2014;75:5-42.

[19] Sharma S, Pollet BG. Support materials for PEMFC and DMFC electrocatalysts—A review. Journal of Power Sources. 2012;208:96-119.

[20] Shao Y, Zhang S, Kou R, Wang X, Wang C, Dai S, et al. Noncovalently functionalized graphitic mesoporous carbon as a stable support of Pt nanoparticles for oxygen reduction. Journal of Power Sources. 2010;195:1805-11.

[21] Julkapli NM, Bagheri S. Graphene supported heterogeneous catalysts: An overview. International Journal of Hydrogen Energy. 2015;40:948-79.

[22] Soldano C, Mahmood A, Dujardin E. Production, properties and potential of graphene. Carbon. 2010;48:2127-50.
[23] Marinkas A, Arena F, Mitzel J, Prinz GM, Heinzel A, Peinecke V, et al. Graphene as catalyst support: The influences of carbon additives and catalyst preparation methods on the performance of PEM fuel cells. Carbon. 2013;58:139-50.
[24] Antolini E. Graphene as a new carbon support for low-temperature fuel cell catalysts. Applied Catalysis B: Environmental. 2012;123-124:52-68.
[25] Seger B, Kamat P. V. Electrocatalytically Active Graphene-Platinum Nanocomposites. Role of 2-D Carbon Support in PEM Fuel Cells. The Journal of Physical Chemistry C Letters.2009;113:7990-7995.
[26] Park S, Shao Y, Wan H, Rieke PC, Viswanathan VV, Towne SA, et al. Design of graphene sheets-supported Pt catalyst layer in PEM fuel cells. Electrochemistry Communications. 2011;13:258-61.
[27] Brownson DAC, Kampouris DK, Banks CE. An overview of graphene in energy production and storage applications. Journal of Power Sources. 2011;196:4873-85.
[28] Geng Y, Wang SJ, Kim JK. Preparation of graphite nanoplatelets and graphene sheets. J Colloid Interface Sci. 2009;336:592-8.
[29] Wang G, Yang J, Park J, Gou X, Wang B, Liu H, Yao J. Facile Synthesis and Characterization of Graphene Nanosheets. J. Phys. Chem. C. 2008;112:8192-8195.
[30] Stankovich S, Dikin DA, Piner RD, Kohlhaas KA, Kleinhammes A, Jia Y, et al. Synthesis of graphene-based nanosheets via chemical reduction of exfoliated graphite oxide. Carbon. 2007;45:1558-65.
[31] Dreyer DR, Park S, Bielawski CW, Ruoff RS. The chemistry of graphene oxide. Chem Soc Rev. 2010;39:228-40.
[32] Xin Y, Liu J-g, Zhou Y, Liu W, Gao J, Xie Y, et al. Preparation and characterization of Pt supported on graphene with enhanced electrocatalytic activity in fuel cell. Journal of Power Sources. 2011;196:1012-8.
[33] Daş E, Alkan Gürsel S, Işıkel Şanlı L, Bayrakçeken Yurtcan A. Thermodynamically controlled Pt deposition over graphene nanoplatelets: Effect of Pt loading on PEM fuel cell performance. International Journal of Hydrogen Energy. 2017;42:19246-56.
[34] Quesnel E, Roux F, Emieux F, Faucherand P, Kymakis E, Volonakis G, et al. Graphene-based technologies for energy applications, challenges and perspectives. 2D Materials. 2015;2.
[35] Zhang Y, Erkey C. Preparation of supported metallic nanoparticles using supercritical fluids: A review. The Journal of Supercritical Fluids. 2006;38:252-67.
[36] Bozbağ SE, Erkey C. Supercritical deposition: Current status and perspectives for the preparation of supported metal nanostructures. The Journal of Supercritical Fluids. 2015;96:298-312.
[37] Daş E, Kaplan BY, Gürsel SA, Yurtcan AB. Graphene nanoplatelets-carbon black hybrids as an efficient catalyst support for Pt nanoparticles for polymer electrolyte membrane fuel cells. Renewable Energy. 2019;139:1099-110.
[38] Bozbağ SE, Gümüşoğlu T, Yılmaztürk S, Ayala CJ, Aindow M, Deligöz H, et al. Electrochemical performance of fuel cell catalysts prepared by supercritical deposition: Effect of different precursor conversion routes. The Journal of Supercritical Fluids. 2015;97:154-64.
[39] N. I. Kovtyukhova, P. J. Ollivier, B. R. Martin, T. E. Mallouk, S. A. Chizhik, E. V. Buzaneva and A. D. Gorchinskiy, Layer-by-Layer Assembly of Ultrathin Composite Films from Micron-Sized Graphite Oxide Sheets and Polycations, Chem. Mater. 1999 (11) 771-778.
[40] Bayrakçeken Yurtcan A, Daş E. Chemically synthesized reduced graphene oxide-carbon black based hybrid catalysts for PEM fuel cells. International Journal of Hydrogen Energy. 2018;43:18691-701.

[41] Daş E, Alkan Gürsel S, Işikel Şanli L, Bayrakçeken Yurtcan A. Comparison of two different catalyst preparation methods for graphene nanoplatelets supported platinum catalysts. International Journal of Hydrogen Energy. 2016;41:9755-61.
[42] Bayrakçeken A, Cangül B, Zhang LC, Aindow M, Erkey C. PtPd/BP2000 electrocatalysts prepared by sequential supercritical carbon dioxide deposition. International Journal of Hydrogen Energy. 2010;35:11669-80.
[43] Brunauer S, Emmett P. H, Teller E. Adsorption of Gases in Multimolecular Layers. Journal of the American Chemical Society. 1938;60:309-319.
[44] Saquing CD, Cheng TT, Aindow M, Erkey C. Preparation of platinum/carbon aerogel nanocomposites using a supercritical deposition method. J. Phys. Chem. B. 2004;108:7716-22.
[45] Lebedeva NP, Janssen GJM. On the preparation and stability of bimetallic PtMo/C anodes for proton-exchange membrane fuel cells. Electrochemica Acta 2005;51:29-40.
[46] Mikhailov S. Physics and Applications of Graphene Experiments. ISBN: 978-953-307-217-3. Chapter 17, page 423.
[47] Yu S, Liu Q, Yang W, Han K, Wang Z, Zhu H. Graphene-CeO2 hybrid support for Pt nanoparticles as potential electrocatalyst for direct methanol fuel cells. Electrochim. Acta. 2013;94:245-251.
[48] Hasa B, Martino E, Vakros J, Trakakis G, Galiotis C, Katsaounis A. Effect of Carbon Support on the Electrocatalytic Properties of Pt–Ru Catalysts. ChemElectroChem. 2019;6:4970-9.
[49] Memioğlu F, Bayrakçeken A, Öznülüer T, Ak M. Synthesis and characterization of polypyrrole/carbon composite as a catalyst support for fuel cell applications. International Journal of Hydrogen Energy. 2012;37:16673-9.
[50] Schonvogel D, Hülstede J, Wagner P, Kruusenberg I, Tammeveski K, Dyck A, et al. Stability of Pt Nanoparticles on Alternative Carbon Supports for Oxygen Reduction Reaction. Journal of The Electrochemical Society. 2017;164:F995-F1004.
[51] Tarasevich M.R, Bogdanovskaya V. A, Zagudaeva N. M. Redox Reactions of Quinones on Carbon Materials. J. Electroanal. Chem. 1987;223:161-169.
[52] Şanlı LI, Bayram V, Yarar B, Ghobadi S, Gürsel SA. Development of graphene supported platinum nanoparticles for polymer electrolyte membrane fuel cells: Effect of support type and impregnation–reduction methods. International Journal of Hydrogen Energy. 2016;41:3414-27.

Atatürk Üniversitesi
Anadolu Fizik ve Astronomi Dergisi
(ISSN: 2791-8718)
Cilt 2, Sayı 1, 18-27
Atatürk University
Journal of Anatolian Physics and Astronomy
(ISSN: 2791-8718)
Volume 2, Issue 1,18-27

JAPA

Spectral Disentangling of Binary Stars: ε Lupi

[*1]Vildan Dizdaroğlu, [2]Ahmet Dervişoğlu

[*1]Erciyes University, Graduate School of Natural and Applied Sciences, Kayseri, Turkey.
[2]Ataturk University, Astronomy and Space Sciences Department, Erzurum, Turkey.

ORCID[*1]: https://orcid.org/0000-0002-5166-0282

Research Type: Research Article
Received: 23.03.2022, Accepted: 28.04.2022
*Corresponding author: vildan.dizzdar@gmail.com (V. Dizdaroğlu)

Abstract

In this study, which is based on spectral disentangling in binary systems, ε Lupi (HD 136504) has been studied. ε Lupi is a double-lined spectroscopic binary system (SB2) consisting of two early type B stars. A total of 575 spectra of ε Lupi downloaded from the PolarBase database were used for spectral disentangling. Before spectral disentangling, we cleaned telluric lines, merged orders, normalized the continuum of spectra. To obtain individual spectra of the components, FDBinary code was used. Consequently, the spectra of the components of the ε Lupi system were separated in the wavelength range 3920 - 8560 Å. The radial velocities and atmospheric parameters of the primary and secondary components will be found using with the resultant normalized spectra of ε Lupi.

Key Words: Binary stars, Spectral disentangling, ε Lupi, Spectral analysis.

Çift Yıldızlarda Tayfsal Çözümleme: ε Lupi

Özet

Çift yıldız sistemlerinde tayfsal çözümleme konusunu ele alan bu çalışmada, ε Lupi (HD 136504) yıldızı incelenmiştir. ε Lupi iki erken tür B yıldızından oluşan çift çizgili tayfsal çift (SB2) sistemdir. Tayfsal çözümleme için ε Lupi'ye ait PolarBase arşivinden indirilen toplam 575 tayf kullanılmıştır. Çift sisteme ait bileşen tayfları ayırmadan önce tellürik çizgileri temizleme, tayf parçalarını(order) birleştirme, süreklilik normalizasyonu vb. işlemler uygulanmıştır. ε Lupi'ye ait bileşen tayfların ayrı ayrı elde edilmesi için FDBinary kodu kullanılmıştır. Sonuç olarak, ε Lupi'nin bileşen tayfları 3920 - 8560 Å dalgaboyu aralığında ayrılmıştır. Bu çalışma sonucunda ε Lupi'nin bileşenlerine ait normalize tayflar kullanılarak dikine hızlar ve atmosferik parametreler bulunabilir.

Anahtar Kelimeler: Çift yıldızlar, Tayfsal çözümleme, ε Lupi, Tayf analizi.

1. Introduction

Son yıllarda çift yıldızların analizi için birçok yöntem geliştirilmiştir. İlk olarak 1994 yılında Simon & Sturm yaptıkları çalışma ile yörünge faz aralığını kapsayan gözlemlerden çift çizgili tayfsal ikiliden bileşen yıldıza ait olan tayfı çıkarabildiği tayfsal çözümleme (SPD) tekniğini bulmuştur [1]. Bu teknik SPD çizgilerinin iç içe geçmesinden etkilenmeyen tayfsal yörüngeleri ölçmek için kullanılmaktadır. Ortaya çıkan ayrık tayflar ayrıca orijinal gözlemlerden çok daha yüksek bir sinyal/ gürültü oranına (S/ N) sahiptir, bu da onları kimyasal bolluk analizi için çok yararlı kılmaktadır [2]. Daha sonra Hadrava tarafından 1995 yılında önerilen ve iç içe geçmiş (kompozit) tayfların ayrılması için DFT (Discrete Fourier Transform) yöntemi kullanılmıştır [3]. Bu çalışmanın ardından Sasa Ilijic (2003) çift yıldızların iç içe geçmiş tayflarının çözümlemesi için FDBinary kodunu geliştirmiştir [4]. Unix işletim sistemi için C programlama dilinde yazılan bu kod, Fourier alanında çalışımaktadır.

Thackeray'a göre [5], ε Lupi keşfi, Lick Southern Gözlemevinden 1907-1911 yılları arasında alınan 10 plaka görüntüsü ile Paddock tarafından yapılmıştır [6]. Ancak başkaları tarafından tek hız ölçümleri yapılırken 1907'de H.D. Curtis [7], çift çizgilerin dikine hızlarını (Radial Velocity RV) ölçerek kaydetti. Böylece ε Lupinin çift çizgili tayfsal çift yıldız olduğu gözlendi. 1964 yılında Radcliffe Gözlemevinde tayf gözlemleri kullanılarak ε Lupinin yörünge parametrelerini elde etmek için çalışmalara başlandı. ε Lupinin çift çizgili davranışına rağmen üretilen ilk yörüngesi bulunmuştur. ε Lupinin yörünge parametrelerinin belirlenmesini zorlaştıran üç durum vardı: (i) Alınan iki tayfın farklı akıda olması, (ii) sistemin bir yörünge döneminin çeyreğinden daha az zamanda, 100 km s^{-1} daha fazla olması, (iii) bileşenlerin ayrıklığının 160 km s^{-1} aşmayan hızlara sahip olması. Bunlara rağmen Thackeray (1970) Radcliffe tayflarını kullanarak ε Lupi'ye ait yörünge parametrelerini elde etmiş ve bu parametreler Tablo 1'de verilmiştir. Tablo 1'de baş ve yoldaş yıldıza ait P (dönem) değerinin olması sistemin tutulma göstermemesinden ve sadece tayfsal çift sistem olmasından kaynaklanır.

Tablo 1: ε Lupi sisteminin Thackeray (1970) tarafından bulunan yörünge parametreleri.

Parametreler	Baş yıldız	Yoldaş yıldız	Toplam sistem
P	4.559794±0.000013	4.559748±0.000026	4.559783 gün
T_0			39370.68±0.09
γ	+7.4±1.94	+6.6±3.7	+7.9±1.4 km s^{-1}
K_1	56.5±2.3		56.1±1.5 km s^{-1}
K_2		65.3±2.8	64.8±1.8 km s^{-1}
e	0.28±0.045	0.21±0.06	0.26±0.03
ω_1	324±11		330±10°
ω_2		171±24	
T	2439370.64±0.10	2430370.85±0.24	2439370.68±0.09

2. Material and Methods

Çift sistemlerin bileşenleri optik teleskoplarla doğrudan gözlemlenemez ve çözülemez. Fotometrik olarak ayrılabilen bazı görsel çift yıldızlar bileşen tayflarının ayrı ayrı kaydedilmesine izin vermeyebilir [4]. Çift yıldız sistemlerinin hemen hemen hepsinde bileşen yıldızların parlaklığı çok farklı olmadığı müddetçe gözlenen tayf her iki bileşene ait özellikler barındırır. Yörünge dönemi boyunca düzenli zaman aralıklarında alınan bu tayflar, bileşen yıldızların dikine hızlarının yörünge dönemine bağımlılığı ve tayf özellikleri hakkında bilgi içerir.

Bileşen yıldızların kütlelerinin belirlenmesi için sistemdeki bileşenlerin yörünge hareketi nedeniyle tayf çizgilerindeki kaymalara bakılır. Ölçülen dikine hız profillerine uygulanan Gauss fiti yapılması gibi basit yöntemler ve çapraz korelasyon (cross-corelation) teknikleri gibi o kadar basit olmayan yöntemler standart dikine hız ölçüm araçları olarak kabul edilir [8]. Ancak çizgilerin karışması, bileşen karışıklığı, sinyal/ gürültü oranı gibi zorluklar bu tür ölçümler için engel teşkil eder. Çapraz korelasyon tekniğinin uygulanması ile büyük bir ilerleme yaşanmıştır. Ancak bu tekniğin dahi (üretilen sentetik tayflar veya belirli tayf türüne ait olan bilinen bir yıldızın tayfı gibi şablon tayflara olan ihtiyaç vb.) dezavantajı vardır. Yüzey sıcaklıklarının belirlenmesi veya yıldız atmosferindeki kimyasal element bolluklarının incelenmesi gibi durumlarda sistemdeki bileşen yıldızların tayflarına ihtiyaç vardır. Elde edilen bu karma karışık bilgiler içeren tayf çizgilerinin ayrılması ve çözülmesi gerekir. Bu zorlukları gidermek için kullanılan bazı yöntemler vardır.
Bunlar; (i) Spektroastrometrik Yarılma (Spectroastrometric Splitting), (ii) Tayfsal Ayırma (Spectral Separation), (iii) Tayfsal Çözülme (Spectral Disentangling) [9]. Yıldız tayflarını ayrı ayrı elde edebilmek ve yörünge parametrelerini daha doğru bir şekilde hesaplayabilmek adına bu çalışmada tayfsal çözümleme tekniği baz alınmıştır.

2.1. Tayfsal Çözümleme (Spectral Disentangling, SPD)

SPD ile iç içe geçmiş tayfların ayrılması, sadece bileşen yıldızların tayflarının yeniden yapılandırılmasına değil, aynı zamanda yıldız sisteminin yörünge parametrelerinin belirlenmesine yönelik bir uygulamadır.

Yörünge elemanlarını elde etmek için ilk uygulamalarda bile, SPD tekniğinin diğer yöntemlerden daha üstün olduğu bulunmuştur [1][10,11]. Sistemin iç içe geçmiş (kompozit) tayflarının her bir bileşen tayfı için doğru ışık faktörleri yani bileşenlerin toplam ışınıma ne kadar katkıda bulundukları ve dikine hızları bilinmelidir. Bu bileşenler bilindiği takdirde iç içe geçmiş tayfların yeniden yapılandırılması ve bileşenlerine ayrılması mümkündür. Işık faktörleri, ışık eğrilerinin analizi ile belirlenebilir. Dikine hızlar, Gaussları iyi çözülmüş çizgilere yerleştirilmesi gibi geleneksel teknikler yoluyla veya iki boyutlu çapraz korelasyon yoluyla doğrudan iç içe geçmiş tayfta ölçülebilir.

İç içe geçmiş tayfların ayrılması için ışık oranı hakkında önceden bir bilgi sahibi olmamız gerekmez ancak dikine hızların yanlış belirlenmesi bileşen tayfları çözerken büyük bir sorun teşkil eder. Bu nedenle, doğru dikine hızlar, yıldız sisteminin bireysel bileşenlerinin tayflarını yeniden yapılandırmak için gereken iç içe geçmiş tayflar olan verilerin ikinci en kritik kısmı olarak düşünülebilir. SPD ile ölçülen yörüngeler tutarlıdır ve karmaşık çizgiler için herhangi bir düzeltme

gerekmez. Bu bakımdan SPD tekniğinin uygulanması teşvik edicidir. Bu yüzden bu çalışmada ε Lupi sistemine SPD tekniği uygulanmıştır.

2.2. FDBinary Kodu

FDBinary, çift yıldızların iç içe geçmiş tayflarının ayrılması ve çözülmesi için kullanılan açık kaynaklı bir koddur. SPD dikine hızları kullanarak Fourier uzayında uygulanır. Ayrıca Keplerin yörünge elemanlarından beş parametreye bağlıdır: (i) bileşenlere ait dikine hız yarı genliği, (ii) dış merkezlik, (iii) genel bir evre kayması ve (iv) enberi boylamı. Yörünge hareketlerini açıklayan bu parametrelere ek olarak iki parametre kullanılabilir. Bu iki parametre ise Gözlenen girdi tayfları ve yörünge dönemidir. Gözlenen girdi tayfları, dalgaboyunda seçilen aralıklarla logaritmik ölçekte örneklenmelidir. Yörünge dönemi, gözlemlenen her bir tayfta belirlenmelidir.

SPD tekniğinin uygulanmasında kullandığımız *FDBinary* kodu hız uzayında ve matris formatında çalışır. Bu kodu farklı zamanlarda ve farklı dalgaboyu aralıklarında alınmış çift yıldız sistemine ait bileşke tayflarını ayrı ayrı elde edilmesini sağlar. *FDBinary* kodunun akış şeması Şekil 1'de verilmiştir.

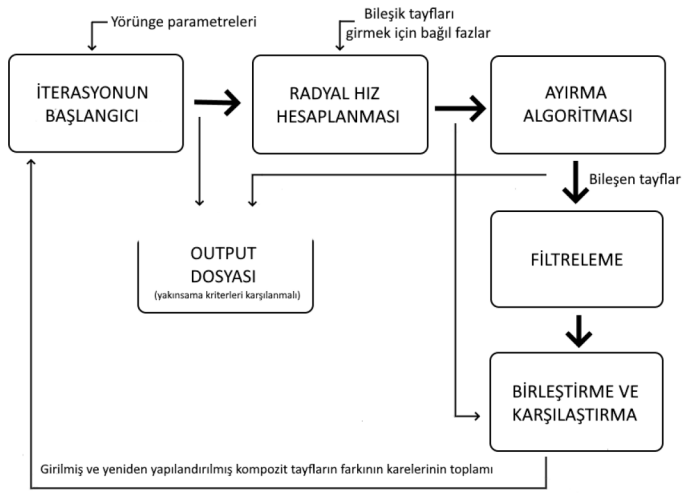

Şekil 1. FDBinary kodunun akış şeması

FDBinary kodu girdi (input) ve çıktı (output) dosyalarından oluşur. Girdi dosyasında verdiğimiz parametrelere göre bu kod iterasyon yaparak çıktı dosyasını oluşturur ve bize bileşen yıldızlara ait ayrılmış tayfaları verir.

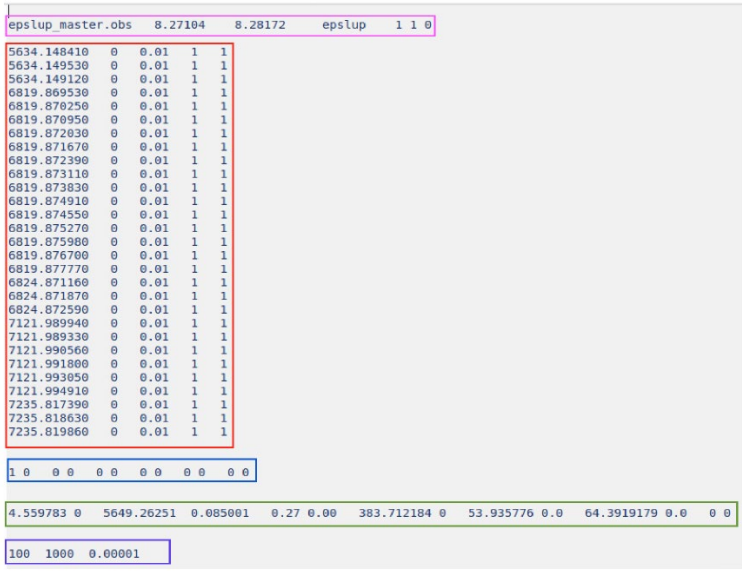

Şekil 2. ε Lupi'ye ait FDBinary için hazırlanan input dosyası.

Oluşturulan girdi dosyası, gözlenen tayflar için yörünge parametreleri ve girilen ilk değerler gibi tanımlayıcıları içeren kontrol dosyasıdır. Zamanlar gün, hızlar km s^{-1} ve açılar derece cinsindendir. Şekil 2'de verilen örnek girdi dosyasının içinde bulunan 'epslup_master.obs' isimli dosyada sisteme ait gözlenen tayflar bulunur. Bu dosyada, çift sisteme ait tayfların dalgaboyuna (logaritmik ölçekte) karşılık normalize akı değerlerini içeren matris formatında veriler bulunur. 'epslup' ise çözümleme için kullanılan dalgaboyu aralığındaki gözlemleri içeren çıktı (output) dosyasıdır. Şekil 2'de bulunan pembe kutunun içindeki değerler sırasıyla gözlem tayfları, çözümleme yapılacak dalgaboyu aralığı, çıktı dosyası ve yıldız sistemine ait bileşen değerleridir. Kırmızı kutunun içinde tanımlananlar gözlenen tayfa ait özellikleri içerir. Sırasıyla sütunlarda bulunan değerler: gözlemlere ait Jülyen günü (JD), güneş merkezli dikine hız düzeltmesi, hata payı, baş yıldıza ait ışık faktörü ve yoldaş yıldıza ait ışık faktörü. Mavi kutunun içindeki değerler üçüncü bileşene ait değerlerdir. Yeşil kutunun içindeki değerler iç yörüngeye ait parametreleri içerir. Bu değerler; dönem (P), başlangıç zamanı (T0), dış merkezlik/basıklık (e), yıldızın koç noktasından enberi noktasına olan açısı (ω), baş yıldızın dikine hızı (K1) ve yoldaş yıldızın dikine hızı (K2) şeklindedir. Son olarak mor kutunun içindekiler ise sırasıyla kalibre sayısı, iterasyon ve toleranstır.

SPD yapılacak olan yıldıza ait parametreler ile oluşturulan girdi dosyasının hazırlanmasıyla *FDBinary* kodu çalıştırılır. Bu kod verilen ilk değerleri kullanarak iterasyon yapar ve çift yıldıza ait tayfları ayırır. Bu işlemin tamamlanmasıyla bu kod bize ayrılmış tayflara ait çıktı dosyalarını verir.

3. Tartışma ve Bulgular

PolarBase yıldız arşivinden sıcaklıkları 10000-40000 K arasındaki çift yıldız sistemlerini incelenmiştir. İncelenen bu yıldızlardan SPD için uygun görülen ε Lupi çift yıldız sistemi üzerinde çalışmaya karar verilmiştir. PolarBase yıldız arşivinden ε Lupi'ye ait normalize edilmemiş tayflara ait veriler indirilmiştir. İndirilen verilerden Jülyen günleri ile Tablo 1'deki sonuç sütununda yer alan P ve T0 değerlerini alarak *FDBinary* sonucunda elle ettiğimiz dikine hızlar ile ε Lupi'ye ait tayfların evre

dağılımına göre dikine hızları hesaplanmıştır (Şekil 3). Çift yıldızların iki bileşeninden aynı anda 0.25 ve 0.75 evrelerinde tayf bilgisi alındığından dolayı ε Lupi'nin bu evreler civarından tayfının olup olmadığını kontrol edilmiştir. Evre dağılımını iyi anlayabilmek için hesaplanan evrelerin dikine hız eğrisi oluşturulmuştur.

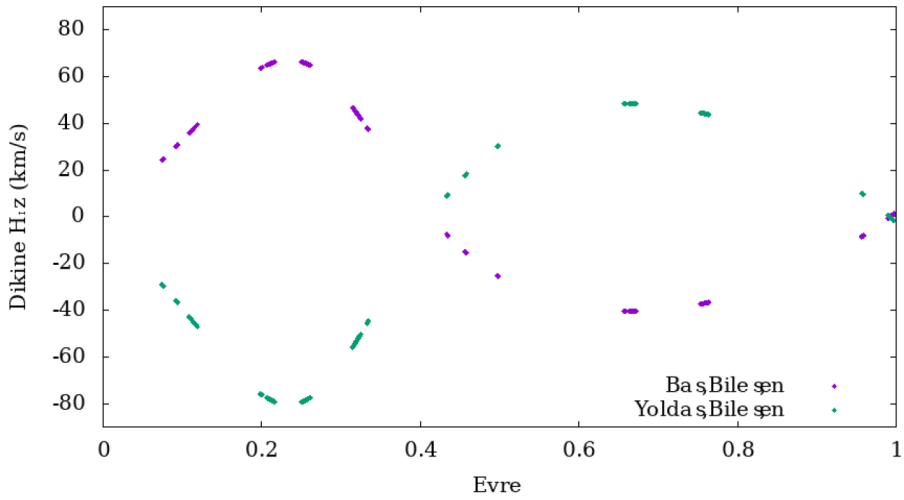

Şekil 3. PolarBase arşivinden indirilen 575 tane tayf kullanılarak oluşturulan ε Lupi'ye ait dikine hız eğrisi. Sistemdeki baş(mor) ve yoldaş(yeşil) bileşene ait tayf çizgilerinin dikine hız ölçümleri verilmiştir. x-ekseninde evreye karşı y-ekseninde dikine hız değerleri verilmiştir.

Tayfsal ayırmanın ilk aşaması olarak, ε Lupi'ye ait indirdiğimiz tayfların içindeki verilerde eksiklik olup olmadığı incelenmiştir. Bunun sonucunda 568 tayfın kullanılabilir olduğuna karar verilmiştir. Bu tayfları normalize etmek için yazmış olduğumuz normalizasyon kodu kullanılmıştır. Bu kodu kullanmadan önce iSpec yardımıyla ε Lupi'ye ait atom çizgilerinin tayf üzerindeki konumlarını dalgaboyuna göre belirleyerek çizgi listesi oluşturulmuştur. Oluşturduğumuz bu çizgi listesini, atom çizgilerinin sürekliliğinin bozulmaması için normalizasyon kodunda kullanılmıştır. Normalizasyon koduyla: (i) Atmosferden kaynaklı etkilerden oluşan tellürik çizgileri tayftan temizledik, (ii) sürekliliği bulmak için tayf parçalarının (order) akı değerinin maksimum ile minimumdaki dalga boyunu ve medyan değerlerini belirledik, (iii) belirli dalgaboyu aralıklarındaki tayf parçalarına sırasına göre normalize ettik. Normalizasyon sonucu elde ettiğimiz tayf parçalarını birleştirilirken bazı sorunlar meydana geldi. Birleşmiş tayfta, tayf parçalarının kenarları üst üste gelerek sürekliliğin akı kalınlaşmasına neden oldu. Bu sorunu giderebilmek için tayf parçalarını dalgaboyuna göre kırpılmıştır. Ardından tayf parçalarının ortalamasını ve medyanını alarak tekrar normalize edilmiştir. En sonunda tüm tayf parçaları birleştirilmiştir. Birleştirdiğimiz tayf parçaları Şekil 4'te sunulmuştur.

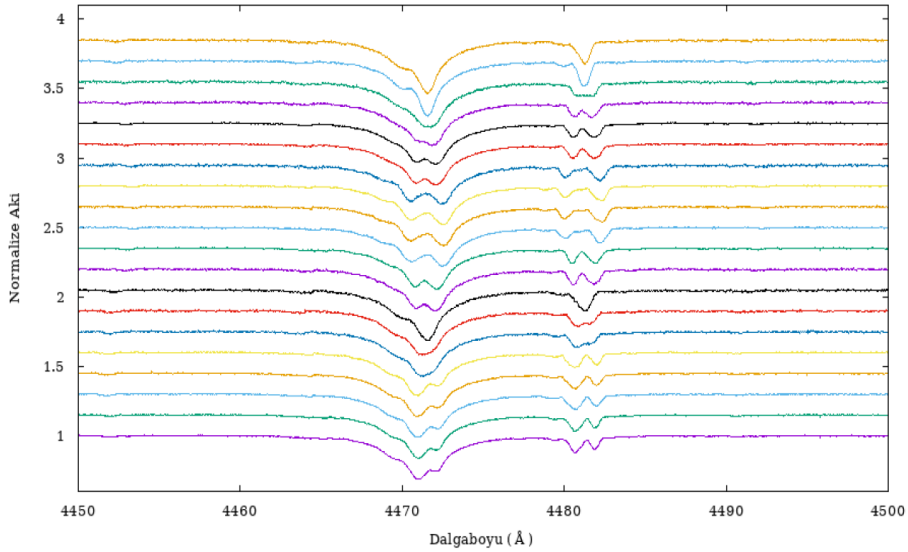

Şekil 4. ε Lupi'ye ait farklı evrelerde alınmış 20 tayfın dalgaboyuna karşılık normalize akı grafiği. Burada Helyum (4471 Å) ve Magnezyum II (4481 Å) çizgilerinin evreye göre değişimi rahatlıkla fark edilmektedir.

Normalize ettiğimiz tayfları incelediğimizde Balmer Serisinin iyi bir şekilde normalize olmadığını fark ettik. Bu durum Balmer çizgilerinin geniş olmasından kaynaklanır. Bu etkinin sonucunda süreklilik normalizasyonunda kaymalar meydana gelir. Bu sorunun giderilmesi için hidrojen çizgilerine farklı bir normalizasyon işlemi uyguladık. Örnek olarak Şekil 5'te yeniden normalize edilmiş H*γ* çizgisi iSpec üzerinden gösterdik.

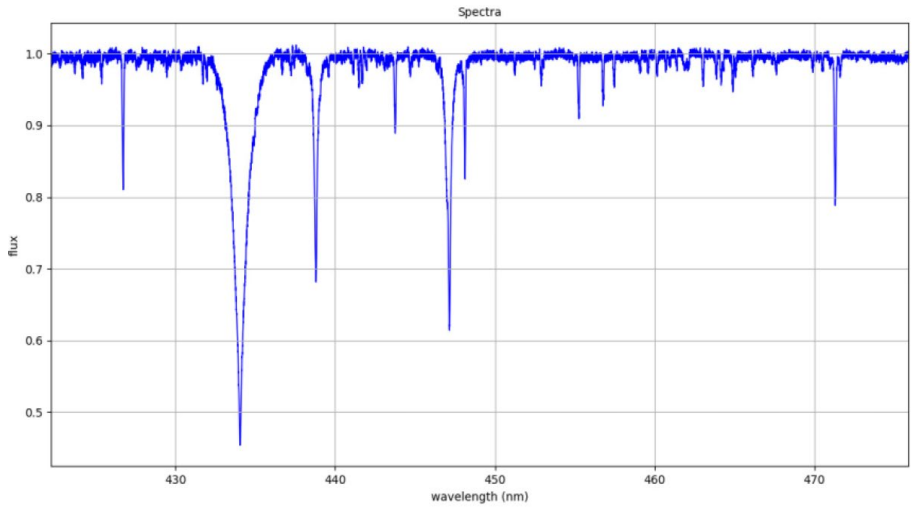

Şekil 5. Yeniden normalize edilmiş H*γ* çizgisinin dalgaboyuna (wavelength) karşılık akı (flux) değerinin iSpec arayüzünde gösterimi. Dalgaboyu nanometre (nm) birimindedir. H*γ* çizgisi 434.1 nanometreye karşılık gelir.

ε Lupi sistemine ait yıldızların tayflarını ayrı ayrı elde etmek için incelenen tayfların *FDBinary* programında kullanılacak formata dönüştürdük (Ayrıntıları için bkz. bölüm 2.2). *FDBinary* kodu için Şekil 1'deki gibi girdi dosyalarımızı oluşturduk. Bu dosyalar oluşturulurken bileşenlerin ışığa katkı oranları bilinmediğinden ikisi içinde ışık faktörü (lf = 1.0) değerini aldık. ε Lupi'nin normalize edilmiş

tayfını en fazla 30 Å dalgaboyu aralıklarında bölerek kodu çalıştırdık. Bu işlemi Balmer serisi için de ayrıca yaptık. *FDBinary* kodu ile girilen parametrelere göre belirlediğimiz dalgaboyu aralığında iterasyon yaparak ε Lupi'nin bileşenlerinin tayfını ayrı ayrı elde ettik. Sonuç olarak *FDBinary* bize beş çıktı dosyası verdi: (i) '.obs' uzantılı bileşik tayfı, (ii) '.mod' uzantılı bileşen yıldızların ayrılmış tayflarını içeren model tayfı, (iii) '.res' uzantılı ayırma işlemi için belirlediğimiz dalgaboyu aralığındaki kalıntısı, (iv) '.rvs' uzantılı bileşenlerin dikine hız verileri ve (v) '.log' uzantılı yapılan işlemlerin kayıtlarının olduğu dosya. Elde edilen bu dosyalardan '.mod' uzantılı dosyadaki bileşenlere ait model tayfları ayırdık. Sürekliliği normalize etmek için öncelikle iSpec koduyla hazırlanmış gridlerden sentetik tayf oluşturduk. Bunun için B yıldızlarına özel hazırlanan BSTAR2006_TLUSTY sentetik tayf gridlerini kullandık [12]. Ayrıca ε Lupi'ye ait baş ve yoldaş yıldızın sırasıyla yüzey çekim ivmeleri loggAa = 3.97, loggAb = 4.13 ve etkin sıcaklıkları için sırasıyla Teff Aa = 20500 K, Teff Ab = 18500 K ile tayf çözünürlüğü için de R = 85000 piksel kullandık.

Oluşturulan sentetik tayfı *Java Multipeagle* programında kullanarak, *FDBinary*'den elde edilen tayfların sürekliliğini normalize ettik. Bu işlem sırasında süreklilikteki çakışan kısımların fazlalıklarını atarak birleştirdik. Son olarak baş ve yoldaş yıldıza ait normalize edilmiş ve ayrılmış tayfları Şekil 6 ve Şekil 7'de örnek olarak çizdirdik.

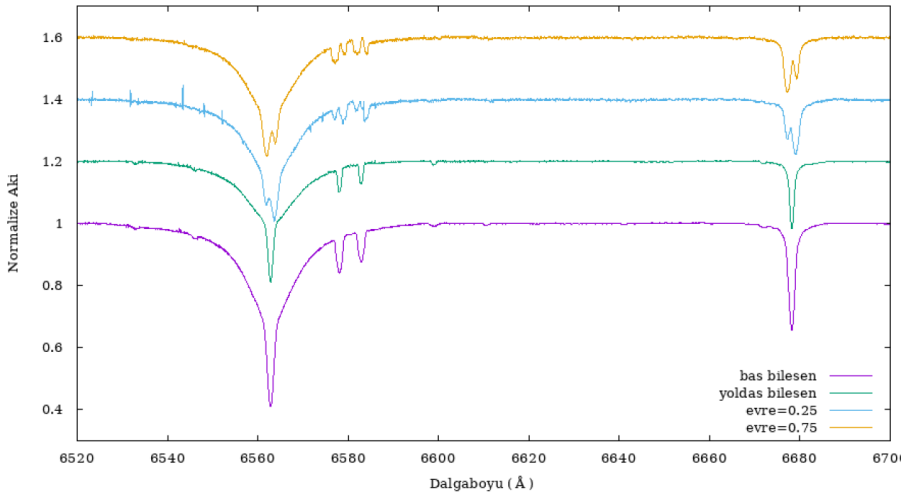

Şekil 6. ε Lupi'ye ait 6520 - 6700 Å dalgaboyu aralığındaki ayrılmış tayfların baş yıldız (mor), yoldaş yıldız (yeşil) ve birleşik tayfın 0.25 (Mavi) ve 0.75 (Sarı) evreden alınan tayfları olmak üzere normalize akıya karşı dalgaboyu grafiği. Grafikte H**α** (6563 Å) ile He I (6678 Å) gösterilmektedir.

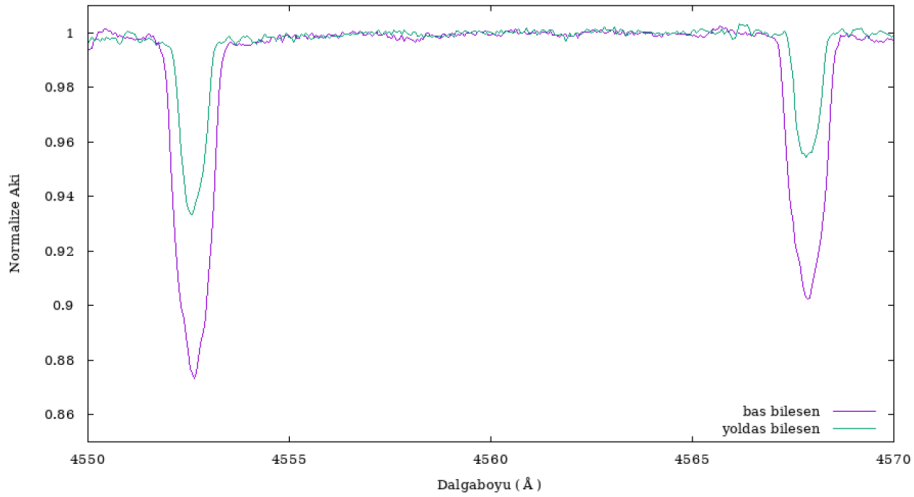

Şekil 7. ε Lupi'ye ait FDBinary kodu ile çözdüğümüz Si III (4553 Å ve 4568 Å) soğurma çizgilerine ait normalize akı değerine karşı dalgaboyu grafiği. Baş yıldız (mor) ve yoldaş yıldız (yeşil) olarak çizdirdik.

4. Sonuç ve Öneriler

Çift yıldız sistemlerinde tayfsal çözümleme konusunu temel alan bu çalışmada, iki erken tip B tayf türünden yıldız içeren ε Lupi (HD 136504) çift çizgili tayfsal çift sistemi kullanıldı. ε Lupi'nin evre dağılımının iyi olması ve daha önce tayfsal ayırma yapılmamış olması bizim için iyi bir aday olduğunu gösterdi.

ε Lupi'ye ait farklı evrelerdeki gözlemlerden çift çizgili tayfsal çiftin bileşenlerine ait olan tayfı ayrıştırmak için tayfsal çözümleme (SPD) tekniğini uyguladık. SPD tekniğini uygularken iSpec programından ve *FDBinary* kodundan yararlandık. Bu çalışma sonucunda ε Lupi sistemine uyguladığımız çözümleme tekniği ile baş ve yoldaş bileşenlerin ayrı ayrı tayflarını elde ettik. Ayrıca Sisteme ait yörünge parametrelerini K_1= 53.8914 km s^{-1}, K_2= 64.6822 km s^{-1}, e = 0.2723, T_0= 2439370.83 JD ve ω= 383°.1 olarak hesapladık.

Çalışma sonucunda elde edilen ayrılmış tayflar kullanılarak yıldızların atmosferik parametreleri belirlenebilir. Ek olarak çalışma sonucunda ε Lupi'ye ait normalize edilmiş tayflara LSD ve CCF yöntemlerini uygulayarak bileşenlerin dikine hızları hesaplanabilir. Bulunan dikine hızlarla bileşenlere ait kütleler elde edilebileceği sonucuna varılmıştır.

Çıkar Çatışması

Yazarlar herhangi bir çıkar çatışması olmadığını beyan etmektedirler.

Kaynaklar

[1] Simon, K. P., Sturm, E., & Fiedler, A. 1994. Spectroscopic Analysis of Hot Binaries. Astronomy and Astrophysics, 292, 507.

[2] Pavlovski, K., Southworth, J., Tamajo, E.,2018. Physical Properties and CNO Abundances for High-Mass Stars in Four Main-Sequence Detached Eclipsing Binaries: V478 Cyg, AHCep, V453Cyg, and V578 Mon. Monthly Notice of the Royal Astronomical Society, 3129-3147.

[3] Hadrava, P. (1995). Orbital elements of multiple spectroscopic stars. Astronomy and Astrophysics Supplement Series, 114, 393.

[4] Ilijic, S., 2003. Spectral Disentangling of Close Binary Stars. University of Zagreb Faculty of Sciences, Degree of master, Zagreb, 65 s.

[5] Thackeray A. D., 1970. The Double-Lined Spectroscopic Binary ε Lupi (HD 136504). Monthly Notice of the Royal Astronomical Society, 149, 75-80.

[6] Campbell, W. W. & Moore, J. H., 1928. PubL Lick Obs. XVI, 223.

[7] Moore, J. H., 1910. Lick Obs. BulLy 6, 151.

[8] Pavlovski, K., Hensberge, H., 2006. Modern Analysis Techniques for Spectroscopic Binaries. International Astronomical Union,136-147.

[9] Pavlovski, K., Hensberge, H., 2010. Reconstruction and Analysis of Component Spectra of Binary and Multiple Stars. Astronomical Society of Pasific, 207-216.

[10] Simon, K. P., & Sturm, E. 1995. Disentangling of Composite Spectra. Astronomy and Astrophysics, 281, 286.

[11] Harmanec, P., et al. 1997. The Eclipsing and Spectroscopic Binary V 436 Persei ≡ 1 Persei. Astronomy and Astrophysics, 319, 867.

[12] Lanz, T., Hubeny, I. 2007. A Grid Of Nlte Line-Blanketed Model Atmospheres Of Early B-Type Stars. ApJS

[13] FDBinary Web Adresi: http://sail.zpf.fer.hr/fdbinary/ (Son erişim tarihi: 16.03.2022)

[14] PolarBase Web Adresi: http://polarbase.irap.omp.eu/ (Son erişim tarihi: 16.03.2022)

[15] iSpec Web Adresi : https://www.blancocuaresma.com/s/iSpec/manual/introduction (son erişim tarihi: 16.03.2022)

[16] Blanco-Cuaresma, S., et al. 2014. Determining Stellar Atmospheric Parameters and Chemical Abundances of FGK Stars with iSpec. Astronomy and Astrophysics, 569, A111.

Atatürk Üniversitesi
Anadolu Fizik ve Astronomi Dergisi
(ISSN: 2791-8718)
Cilt 2, Sayı 1, 28-34
Atatürk University
Journal of Anatolian Physics and Astronomy
(ISSN: 2791-8718)
Volume 2, Issue 1, 28-34

JAPA

Investigation of Natural Silica Minerals from the Kizilirmak with EPR Spectroscopy

[*1]Melek Fidan, [2]Recep Tapramaz, [1]Yusuf Şahin

[*1] Department of Physics, Faculty of Sciences, Ataturk University, 25240 Erzurum, Turkey.
[2] Department of Physics, Faculty of Arts and Sciences, Ondokuz Mayıs University, 55139 Samsun, Turkey.

ORCID[*1]: 0000-0002-8138-1743

Research Type: Research Article

Received: 22.02.2022, Accepted: 29.04.2022

*Corresponding author: mbahadir@atauni.edu.tr (M. Fidan)

Abstract

A silica mineral contained in gravel taking from the Kizilirmak deposit and bearing organic radicals in its structure was investigated by EPR spectroscopy. The type of radicals in the silica mineral determined under different temperatures and different microwave power were by examining the intensity distributions of the EPR lines. In EPR spectra, the signals with different intensity distributions were detected. g and A spin-Hamiltonian parameters for these signals were calculated and given in Table 1. These signals are attributed to the $\dot{C}H_2$, $\dot{C}H_3$, $\dot{C}H$, CO_2^-, O_3^- radicals in the glassy structure by comparing with the literature.

Key Words: EPR, Radical, Glassy structure.

Kızılırmak Yatağından Çıkarılan Doğal Silis Mineralinin EPR Spektroskopisi ile İncelenmesi

Özet

Kızılırmak yatağından alınan çakıl içinde bulunan ve yapısında organik radikaller bulunduran bir silis minerali EPR spektroskopisi ile incelenmiştir. Farklı sıcaklıklarda ve farklı mikrodalga gücü altında incelenen silis minerali içerisindeki radikallerin türü, EPR çizgilerinin şiddet dağılımlarına bakılarak belirlenmiştir. EPR spektrumlarında şiddet dağılımları birbirinden farklı olan sinyaller tespit edilmiş ve bu sinyallere ait g ve A spin-Hamiltonien parametreleri hesaplanmış ve Tablo 1'de verilmiştir. Literatür ile karşılaştırılarak, sinyaller camsı yapı içerisindeki $\dot{C}H_2$, $\dot{C}H_3$, $\dot{C}H$, CO_2^-, O_3^- radikallerine atfedilmiştir.

Anahtar Kelimeler: EPR, Radikal, Camsı yapı.

1. Introduction

The root of natural stones is based on the molten magma of the Earth's core, which constantly moves and always tries to reach the outer surface. Some of this extremely hot mass brings volcanic activity and lava flow. Magma often flows into underground cracks in the lower layer of the planet. Boiling water, steam and gases have also accompanied with the molten rock and minerals. It has been occurring the crystals and precious stones by combining with many minerals that accumulates in the cracks while gasses are become cold.

The surrounding mineral is shaped by pressure, heat and chemically acid or basic media. The small change in environmental conditions can even allow a mineral to grow, stop, change or even form a new one. This may cause to show different properties in the same mineral found in different places [1, 2]. There are many active fault lines in Turkey. There are many different natural phenomena and occurrences around these lines. For example, hot water sources and springs are in these regions. In addition to these, various geological events are also observed in these regions. Granites, syenite, monzonite, quartz diorite, biotite granites are present in the massifs along the Kızılırmak. Marble, fluorite, copper, zinc, chromite and magnesite were also detected in the region. One of these is the SiO_2 mineral in the glassy or the crystal forms (quartz, etc.), which is very common in nature. This mineral, in general called as silica or siliceous compound, present in pure form and it composes precious and semi-precious stones in different colors by keeping various metals in impurities, such as opal or amethyst.

Besides these well-known forms, well-known organic radicals can also be trapped within various silica composite located near moving fault lines as mentioned. There is no accurate information about the trapping mechanisms of most active organic radicals trapped in the cavities formed in the SiO_2 matrix. But the most comment one is, the trapped organic compounds which is in silica composite melted within the fossil deposits such as coal, natural gas or oil leaked due to hot magma approaching the surface in faults are fragmented by exposure to high-energy radiation as radiated from radioactive radon (or someone else) leaked from fault fissures. These chemically important and active radicals have continued their existence almost indefinitely since thousands, perhaps millions of years, despite being exposed to various natural conditions [1].

Electron paramagnetic resonance (EPR) spectroscopy is, as well known, a powerful technique for detecting and analyzing trace amounts of paramagnetic impurities at various temperatures. EPR deals only with transitions between spin states. It is not only the external magnetic field that is effective in spin transition. Local magnetic fields produced in the paramagnetic center also affect the spin transitions. The sources making up the local magnetic fields are the nuclei having non-zero spin and other paramagnetic centers located the orbit of the electron and near, which interacts with the paramagnetic ions. In this way, EPR gives detailed information about the orbit of the paramagnetic ion and its interacting nuclei. It can be comments on by taking advantage of the properties of the EPR spectrum such as line intensity, line position, line width and line splitting.

The hyperfine interaction between the magnetic moment of an electron and the magnetic moment of a nucleus can be studied with various experimental techniques [3]. In Electron Paramagnetic Resonance 0EPR) spectroscopy, hyperfine interactions manifest as line splittings in the spectrum.

Such splittings, originating from copper nuclei with spin I= 3/2, have first been observed by R.P. Penrose in 1949 [4] in a single crystal of a copper doped magnesium tutton salt. Since then, measurements of hyperfine interactions with EPR have developed to an indispensable tool for the study of paramagnetic entities in single crystals, in polycrystals, and in frozen and liquid solutions [5-8]. Hyperfine data are particularly helpful in understanding the electronic and geometric structure of paramagnetic species. They enable one to draw up a detailed mapping of the electron spin density distribution, and contain precise information about the spatial arrangement of the nuclei close to the unpaired electron [9, 10].

Electron paramagnetic resonance (EPR) spectroscopy is, as well known, a powerful technique for detecting and analyzing trace amounts of paramagnetic impurities which is assumed to be reflecting the lattice structure of the host at various temperatures. In this study, the types of radicals are determined by examining a silica mineral containing organic radicals and located in pebbles taken from the bed of the Kızılırmak with an EPR spectrometer. This research is particularly interesting for those who work on natural formations, organic radicals, and spectroscopic techniques. It is estimated that the silica mineral was probably formed by the drift of Kızılırmak along the active North Anatolian fault line.

2. Materials and Method

Silica minerals containing organic radicals were extracted from the Kızılırmak deposit. Samples were cleaned to remove any contamination and sized appropriately for EPR measurements. EPR spectra of minerals are recorded in a magnetic field modulation frequency of 100 kHz by using a Varian E-104 X-band EPR spectrometer. The g values were achieved by comparison with a 2,2-diphenyl-1-picrylhydrazyl (DPPH) sample of g = 2.0036.

3. Results and Discussion

EPR spectroscopy is the most powerful tool known for examining and determining these important radicals, in trace amounts, in the minerals containing silicon dioxide and in the glassy structure. An X- band EPR spectrometer was used through the experimental work. The EPR spectra taken this glassy structure found in nature at room temperature shown in Fig. 1 and at 433 K in Fig. 2. The line widths of the signals represented by A and B are increased by rising the temperature to 433 K and therefore the line amplitudes are decreasing. By increasing the microwave power applied to the sample at this temperature, the EPR signals lost in the spectra due to the high Signal to Noise ratio have become evident.

When the permitted transitions are considered in the EPR, if an unpaired electron interacts with a nucleus having the spin I, $2I + 1$ lines with the identical EPR intensity distributions are observed. If there are n identical nuclei interacting with the unpaired electron, the $2nI + 1$ lines appear, whose intensities are not identical. EPR signal groups with different the intensity distributions were observed in the spectrum given in Fig. 2. Existing more than one radical group with the same intensity

distribution indicate that they are taking place in different chemical environments. The hyperfine spin-Hamiltonian has the form

$$\mathcal{H}_{hfs} = S\bar{\bar{A}}I$$

In first order, the measured hyperfine angular frequency consists of two contributions, the isotropic Fermi contact term;

$$a_{iso} = \frac{8\pi}{3\hbar} g_e \beta_e g_n \beta_n \langle \psi_0 | \delta(r) | \psi_0 \rangle$$

and the electron-nuclear dipole-dipole coupling;

$$A_{ij}^{DD} = \frac{g_e \beta_e g_n \beta_n}{\hbar} \left\langle \psi_0 \left| \frac{3 r_i r_j - \delta_{ij} r^2}{r^5} \right| \psi_0 \right\rangle$$

where ψ_0 is the orbital of the unpaired electron and r_i is a component of the radius vector from the electron to the nucleus. The spin-only coupling tensor A^{DD} is traceless and symmetric [11].

g values and superfine splitting constants (A) were found for every radical appears in this glassy. These values indicate which of the signal is belong to which radical. The measured g and A parameters are given in Table 1.

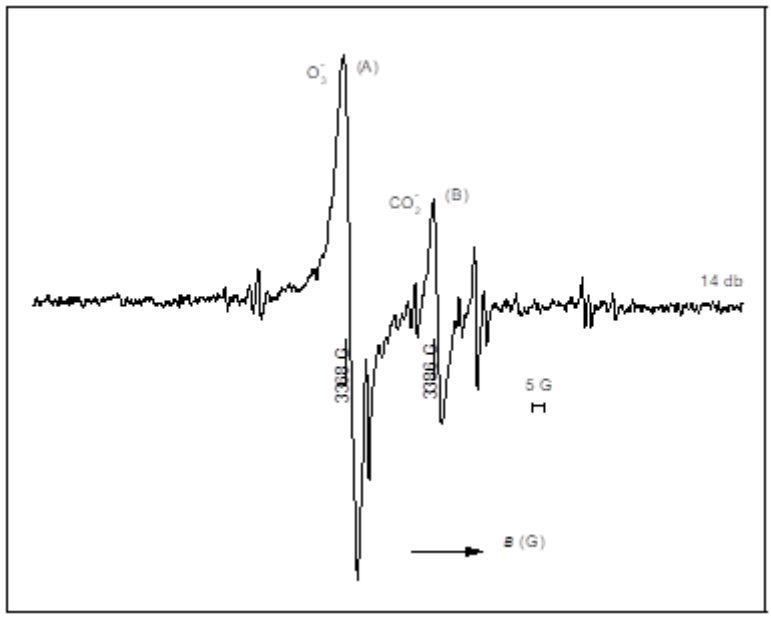

Figure 1. EPR spectrum of natural glassy at room temperature (microwave power= 14 dB).

From the calculated g values of the EPR lines marked as A and B and varied the line widths and intensities as depending on temperature, this EPR signals were determined that belong to O_3^- and CO_2^- radicals, respectively. The g values for these radicals are in agreement with the g values obtained in previous studies [12-14, 17, 22].

Table 1. Spin-Hamiltonien parameters of radicals in natural glassy structure.

Radical	g ± 0.0003	A_1 ± 0.5 (G)	A_2 ± 0.5 (G)	Radical	g ± 0.0003	A_1 ± 0.5 (G)	A_2 ± 0.5 (G)
A	2.0111	-	-	**E**	2.0024	8.75	-
B	2.0002	-	-	**F**	2.0026	22	-
C	2.0018	27	-	**G**	2.0011	123.5	-
D	2.0022	22.5	-	**H**	2.0033	76	5.5

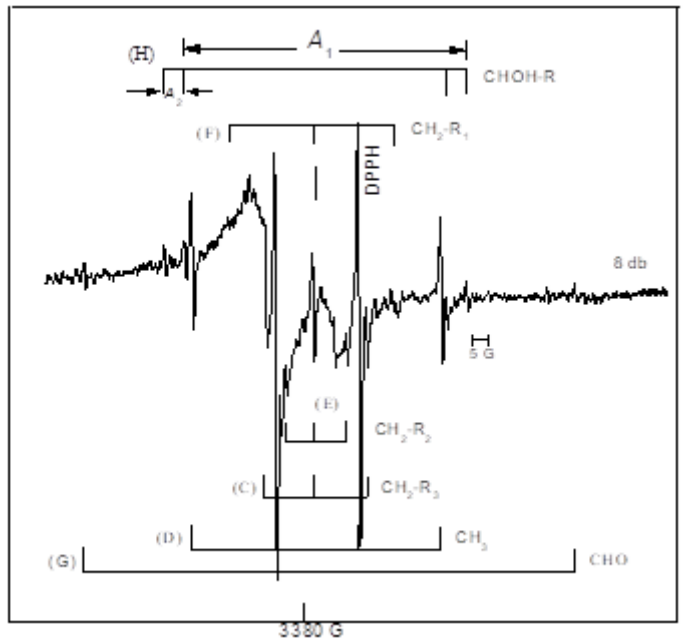

Figure 2. EPR spectrum of natural glassy taken at 433 K (microwave power = 8dB).

The quartet signal (D) shown in Fig. 2 and having a 1: 3: 3: 1 intensity distribution originates from three identical protons of the methyl (• CH_3) group. The g and A values found for this signal is compatible with the literature for the • CH_3 radical [13]. Although the methyl radical is extremely active and mobile, the silica continues its existence in the lattice since thousands of years.

The hyperfine structure splits of the two triplet signals (E and F) in Figure 2 are quite different from each other and the E and F signals have identical shape but belong to two different group in the structure. The g values calculated for these radicals are equal to each other. The difference of hyperfine structure splits is due to CH_2 radicals are linked to different inactive groups [15].

The doublet line indicated by "G" in Figure 2 with the hyperfine splitting of 123.5 G and g = 2.0011 belongs to • HCO radical. The calculated values of g and A for this signal are in good agreement with the published data in the literature [16].

Another doublet with 27 G splitting and g = 2.0018 value appears in Fig. 2. This signal previously represented with a "C" belongs to the • CH_2 radical attached to an inactive group R_3 [18-20]. "H" signal appearing as quadruple signals in the spectrum in Fig. 2 attributed to • CHOH radical. The unpaired electron interacted with one of the non-identical protons and signaled the doublet. The unpaired electron then interacts with the beta proton to cause a doublet repeat splitting [20, 21].

4. Conclusions

The EPR spectra of the natural glassy structures containing silicon are given in Fig. 1 ad Fig. 2. The g values of signals A and B in Figure 1 were determined as 2.0111 and 2,0002 and attributed to radicals O_3^- and CO_2^-, respectively. It was observed that the line widths and intensities of the EPR signals of these radicals changed with temperature. According to the g values of the EPR signals represented by C, D, E, F, G and H in Fig. 2, they can be assigned to the organic radicals • CH_2, • CH_3, CH_2-R_1, CH_2-R_2, • HCO and • CHOH respectively. The spin Hamiltonian parameters of each signal were found and are given in Table 1. The results show that this mineral was probably deposited by the Kızılırmak drifting along the active North Anatolian fault line.

Conflict of Interest

The authors declare that they have no known competing financial interests or personal relationships that could have appeared to influence the work reported in this paper.

References

[1] D.G. Permenov and V.A. Radzig, Mechanism of Heterogenous Processes in the System SiO_2+CH_4, Kinetics and Catalysis, 45 (2004) 293-298.
[2] Sheriff, R.E., Encyclopedic Dictionary of Applied Geophysics, 4th Edition, Geophysical References, Society of Exploration Geophysicists, Vol.13,2002.
[3] Freeman A.J., Frankel R.B. (eds.): Hyperfine Interactions. New York: Academic Press 1967.
[4] Penrose R.P., Nature 163,992 (1949)
[5] Abragam A., Bleaney B.B.: Electron Paramagnetic Resonance of Transition Ions. Oxford: Clarendon Press 1970.
[6] J.E. Wertz, J.R. Bolton, J.A. Weil, Electron Paramagnetic Resonance Elementary Theory and Practical Application, John-Wiley and Sons INC, 568 s, USA, 1993.
[7] Mabbs F.E., Collison D.: Electron Paramagnetic Resonance of d Transition Metal Compounds. Amsterdam: Elsevier 1992.
[8] Pilbrow J.R., Transition Ion Electron Paramagnetic Resonance. Oxford: Clarendon Press 1990.
[9] Chien J.C.W., Dickinson L.C.: Biol. Magn. Reson. 3, 155 (1981)
[10] Hutchison C.A., Appl. Magn. Reson. 3, 219 (1992)
[11] Schweiger A., Concepts for the Measurement of Hyperfine Structure in EPR Spectroscopy, Appl. Magn. Reson. 1993, 5, 229.
[12] J. Kamali and G.N. Walton, Electron Spin Resonance of Gamma, Electron, Neutron and Fission Fragments Irradiated K_2SO_4, Radiated Effects, 84 (1985), 171-184.

[13] R. Köseoğlu, E. Köseoğlu, F. Köksal, E. Başaran, D. Demirci, EPR of Some Irradiated Renal Stones, Radiation Measurements, 40 (2005) 65-68.

[14] F. Callens, P. Matthys, E. Boesman, Paramagnetic Resonance Spectrum of CO_2^- Trapped in KCl, J. Phy. Chem. Of Solids, 50 (1989) 377-381.

[15] N.M. Atherton, Electron Spin Resonance Theory and Application, John-Wiley and Sons INC, 438 s, USA, 1973.

[16] S. Çakır, F. Köksal, R. Tapramaz, O. Çakır, Electron Spin Resonance of Free Radicals in Some Legumes, Cereals and Their Aqueous Solutions Under Photolysis. Radiat. Phys. Chem.,38 (1991), 17-21.

[17] G. Bacquet, V. Quang-Truong, M. Vignoles, J.C. Tromble, G. Bonel, ESR of CO_2^- in X-irradiated tooth enamel and A-type carbonate apatite, Calcif. Tissue Int., 33(1981) 105.

[18] P.W. Atkins and M.C.R. Symons, The Structure of Inorganic Radicals, Elsevier Publishing Company, 1957.

[19] K. Tabaka, J. Jezierska, Molecular Geometry and Hyperfine Interactions in Iminoxy Radicals with C=O or CH_2 Group – DFT and EPR Studies in Liquid and Rigid Media, Chemical Physics Letters, 394 (2004) 298–306.

[20] K. Tabaka, J. Jezierska, Positional and Angular Dependence of Hyperfine Interactions in Cyclic and Bicyclic Iminoxy Radicals with C=O or CH_2 Group – DFT and EPR Studies, Chemical Physics Letters, 410 (2005) 391–399.

[21] F. Köksal, M. Birey, R. Tapramaz, F. Çelik, Journal of Molecular Structure, 211 (1990) 57.

[22] M. Chiesa, E. Giamello, and M. Che, EPR Characterization and Reactivity of Surface-Localized Inorganic Radicals and Radical Ions, Chem. Rev., 110 (2010) 1320–1347.

Atatürk Üniversitesi
Anadolu Fizik ve Astronomi Dergisi
(ISSN: 2791-8718)
Cilt 2, Sayı 1,35 ,42

Atatürk University
Journal of Anatolian Physics and Astronomy
(ISSN: 2791-8718)
Volume 2, Issue 1,35 , 42

JAPA

PHOTOMETRIC OBSERVATIONS of FOUR W UMA BINARIES

[*1]Hüseyin Er, [1]E. Zafer Sönmez, [1]M. Emir Kenger, [1]Necip Karaman, [1]Emre Akkaya, [1]İ. Can Özkesen, [1]Ahmet Polatoğlu

[1]Ataturk University, Faculty of Sciences, Department of Astronomy and Space Science, 25240 Erzurum/Turkey

ORCID[*1]: http://orcid.org/0000-0003-1339-3045

Research Type: Research Article

Received: 28.03.2022 Accepted: 22.04.2022

*Corresponding author: huseyin.er@atauni.edu.tr (H. Er)

Abstract

In this work, the light curves of NSVS2175434, V783 And, ASAS J020753+2034.1 and NR CAM W Uma type eclipsing binary star systems were obtained by using 0.5 meter ATA50 telescope in Atatürk University Astrophysics Research and Application Center (ATASAM). The orbital period variations of the systems were analyzed using the "timing" method. Only the O-C diagram of NR Cam was performed because the eclipse times of the other systems in the literature are not sufficient. When the O-C diagram of the NR Cam system is examined, no clear change has been observed for the time being. However, more observational data are needed to understand whether changes will occur in the future.

Key Words: Binaries, W Uma, Eclipsing stars

DÖRT W UMA ÇİFT YILDIZ SİSTEMİNİN FOTOMETRİK GÖZLEMLERİ

Özet

Bu çalışmada NSVS2175434, V783 And, ASAS J020753+2034.1 ve NR CAM W Uma tipi örten çift yıldız sistemlerinin Atatürk Üniversitesi Astrofizik Araştırma ve Uygulama Merkezi (ATASAM) bünyesindeki 0.5 metrelik ATA50 teleskobu ile elde edilen örtülme ışık eğrileri sunuldu. Sistemlerin yörünge dönem değişimleri "zamanlama" yöntemi kullanılarak incelendi. NR Cam dışındaki sistemlerin literatürdeki minimum zamanları yeterli olmadığı için sadece NR Cam'ın O-C diyagramı oluşturuldu. NR Cam sistemine ait O-C diyagramı incelendiğinde net bir değişime şu an için rastlanılmadı. Ancak ilerleyen zamanlarda değişimin olup olmayacağını daha net görebilmek için daha fazla gözlemsel veriye ihtiyaç vardır.

Anahtar Kelimeler: Çift yıldızlar, W Uma, Örtülme

1. Giriş

Gökyüzünde gördüğümüz yıldızların yarısından fazlası iki veya daha fazla yıldızdan oluşmaktadır. Bu tür sistemler çift yıldız olarak adlandırılmaktadır. Çift yıldız sistemleri, ortak kütle merkezi etrafında kütle çekim etkisi altında Kepler yasalarına göre yörünge hareketi yapan iki veya daha fazla yıldızdan oluşan sistemlerdir [1]. Çift yıldızlarda aralarındaki kütle çekim kuvvetinden yola çıkarak sistemdeki bileşenlerin ışınım gücü, yarıçap ve kütle gibi bazı temel parametreler hesaplanabilir. Bu parametreler yıldızların oluşum süreçleri ve evrim teorileri hakkında bilgi sahibi olmamıza yardımcı olur. Ayrıca, çift yıldızlar yıldız evriminin açıklanmasında, yakın galaksilerin uzaklıklarının belirlenmesinde, X-ışın çiftleri, kataklizmik değişenler, novalar, simbiyotik yıldızlar ve bazı tür süpernovaların açıklanmasında da önemli rol oynamaktadır. Bu nedenle çift yıldızlar, astrofizikte tekli yıldızlara nispeten daha çok bilgi sunmaları bakımından daha büyük bir öneme sahiptirler.

Çift yıldız sistemleri gözlemsel olarak keşfedilme ve incelenme yöntemlerine göre Görsel, Astrometrik, Tayfsal ve Örten çift yıldızlar olarak sınıflandırılır. Örten çift yıldızlarda, sistemdeki bileşenlerden birinin diğerinin önünden geçerken sistemin parlaklığında periyodik bir azalma meydana gelir. Bu nedenle bu tür çift yıldız sistemlerine "Örten Değişen Yıldızlar" adı da verilmektedir [2, 3]. Örten çiftler, ışık eğrilerinin şekillerine göre; Algol türü (EA), β Lyrae türü (EB) ve W UMa türü (EW) sistemler olmak üzere üç ana gruba ayrılırlar. W Uma türü sistemler; farklı kütlelerde, neredeyse aynı sıcaklıklara sahip, birbirine çok yakın ve her ikisi de Roch lobunu doldurmuş yıldızlardan oluşan çift yıldız sistemleri olup bu sistemler aşırı değen örten çiftler olarak da bilinir [2, 4].

Son yıllarda, yapılan araştırmalar sonucunda çift yıldız sistemlerinin yörünge dönemlerinde periyodik olarak bir değişimin olduğu gözlendi [5, 6, 7, 8, 9, 10]. Bu araştırmalar çift yıldız sisteminin kütle merkezinin hareketinden kaynaklanan ve sistemdeki bileşenlerin karşılıklı olarak birbirlerini örtme zamanlarındaki periyodik değişimlerin ölçülmesi sonucu görülen LTT (the Light Travel Time) etkisinin incelenmesiyle yapıldı [8, 11]. LTT etkisi olarak yorumlanan sistemin tutulmalarının O-C (Observed-Calculated) zamanlarındaki periyodik değişimlere dayanan yöntem ise "zamanlama" yöntemi olarak adlandırılmaktadır. Bu çalışmada NSVS2175434, V783 And, ASAS J020753+2034.1 ve NR CAM olmak üzere dört örten W Uma türü çift yıldız sisteminin minimum zamanları hesaplanarak yörüngesel dönemlerinde herhangi bir değişimin olup olmadığı "zamanlama" yöntemi kullanılarak incelendi.

2. Materyal ve Yöntem

NSVS2175434, V783 And, ASAS J020753+2034.1 ve NR CAM W Uma tipi örten çift yıldız sistemlerinin gözlemleri, Atatürk Üniversitesi Astrofizik Araştırma ve Uygulama Merkezi (ATASAM) bünyesindeki 26.3'×26.3' görüş alanına sahip Apogee U230 2K CCD kamera ile 0.5 m'lik (ATA50) teleskop kullanılarak 15 Ekim 2021 ile 16 Kasım 2021 tarihleri arasında her bir kaynak için bir gece olacak şekilde gerçekleştirildi. Tüm sistemlere ait gözlemler, R ve/veya B filtrelerinde ve 20-60 sn aralığında poz süresi verilerek yapıldı.

Temel görüntü indirgeme verileri Bias, Dark ve Flat neredeyse her gözlem gecesi için ayrı ayrı alındı. Veri indirgeme işlemi Python (CCDData, ccdproc, numpy, astropy, matplotlib ve glop gibi paketler) ve MaximDL programları kullanılarak yapıldı. Veri indirgeme işlemi sırasında standart Bias, Dark çıkarımı ve Flat düzeltmeleri yapıldı. Temel amacımız sadece fark ışık ölçümünü elde etmek olduğu için herhangi bir standart yıldız gözlenmedi. Fakat veri indirgeme süresince karşılaştırma yıldızı olarak kaynağa hem parlaklık hem de konum olarak en yakın yıldız kullanıldı (Tablo 1).

Tablo 1 Dört W Uma tipi örten çift yıldızın ve fark ışık ölçümü sırasında kullanılan referans yıldızına ait bilgiler [12]

Kaynak	Kadir	Referans	Kadir
NSVS2175434	13.80 (G)	TYC 4087-1801-1	10.72 (V)
V783 And	14.84 (R)	TYC 2781-920-1	12.44 (B)
ASAS J020753+2034.1	12.85 (V)	TYC 1220-1405-1	11.23 (V)
NR Cam	10.97 (V)	GSC 4531–1979	8.15 (V)

Bu işlemlerin ardından sistemlere ait örtülme ışık eğrileri elde edildi. Sistemlere ait yörünge zaman değişimlerinin incelenebilmesi için elde edilen ışık eğrileri Gauss (Denklem 1) ve Polinom (Denklem 2) fonksiyonları içeren bir fonksiyon (Gauss+Pol) ile modellendi.

Gauss Fonskiyonu:

$$f(x; A, \mu, \sigma) = \frac{A}{\sigma\sqrt{2\pi}} e^{\left[-(x-\mu)^2/2\sigma^2\right]} \qquad Denklem\ 1$$

Polinom Fonksiyonu:

$$f(x; c_0, c_1, \cdots, c_7) = \sum_{i=0,7} c_i x^i \qquad Denklem\ 2$$

Şekil 1a, 1b, 2, 3 ve 4'de görüldüğü gibi elde edilen modellenmiş ışık eğrilerinden dört sistem için de minimum zamanları belirlendi.

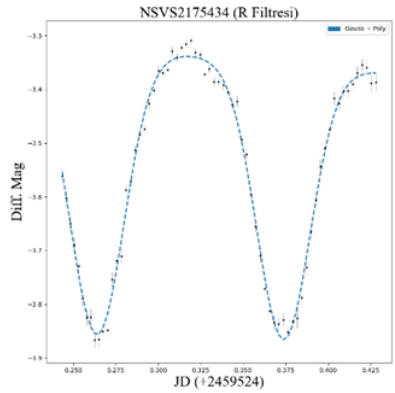

Şekil 1a. NSVS2175434 sisteminin R filtresi kullanılarak ATA50 teleskobu ile yapılan gözleminden elde edilen modellenmiş ışık eğrisi

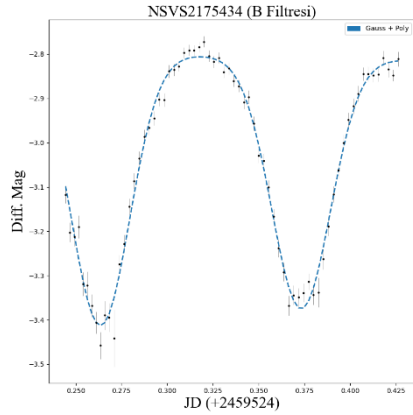

Şekil 1b. NSVS2175434 sisteminin B filtresi kullanılarak ATA50 teleskobu ile yapılan gözleminden elde edilen modellenmiş ışık eğrisi

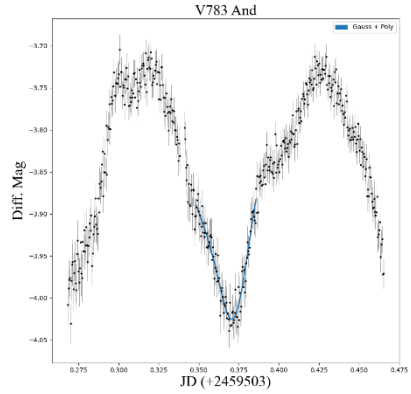

Şekil 2. V783 And sisteminin R filtresi kullanılarak ATA50 teleskobu ile yapılan gözleminden elde edilen modellenmiş ışık eğrisi

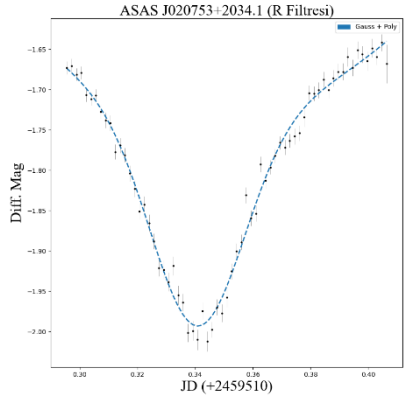

Şekil 3. ASAS J020753+2034.1 sisteminin R filtresi kullanılarak ATA50 teleskobu ile yapılan gözleminden elde edilen modellenmiş ışık eğrisi

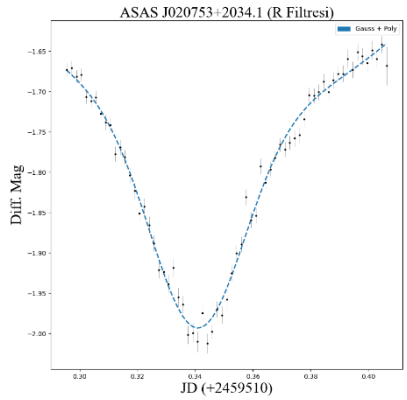

Şekil 4. NR Cam sisteminin R filtresi kullanılarak ATA50 teleskobu ile yapılan gözleminden elde edilen modellenmiş ışık eğrisi

Minimum zamanlar, JD (julian date)'den BJD (barycentric dynamical julian time)'ye dönüştürüldü [13]. Dört sistem için de türetilen minimum zamanları Tablo 2'de gösterildi.

Tablo 2 Dört W Uma sistemine ait elde edilen minimum zamanları

Kaynak	BJD	Hata
V783 And	2459503.37174581	0.0060
ASAS J020753+2034.1	2459510.34073458	0.0038
	2459510.33099462	0.0076
NSVS2175434	2459524.26392948	0.0026
	2459524.37377038	0.0027
	2459524.26353281	0.0036
	2459524.37320581	0.0038
NR Cam	2459535.26596463	0.0010
	2459535.39245006	0.0023

3. Yörünge Dönem Değişimi

Çift yıldız sistemlerinde görülen yörünge dönem değişimini inceleyebilmek için sistemlere ait literatürdeki minimum zamanlar araştırıldı. Ancak O-C diyagramını hazırlayabilmek için V783 And, ASAS J020753+2034.1 ve NSVS2175434 sistemlerine ait yeterli minimum zamanı bulunamadı. Bu nedenle sadece NR Cam için yörünge dönem değişimi incelendi. NR Cam sisteminin, Tavakkoli vd. (2015) tarafından verilen minimum zamanları ile yeni gözlemlerimizden elde edilen minimum zamanları birleştirildi [14]. İncelenen kaynağın yörüngesel dönemlerinde değişim olup olmadığına bakabilmek için her bir kaynağın elde edilen minimum zamanları Şekil 5'deki gibi lineer ışık elemanları ile fit edilir (Denklem 3).

$$BJD = T_0 + P_0 L \qquad Denklem\ 3$$

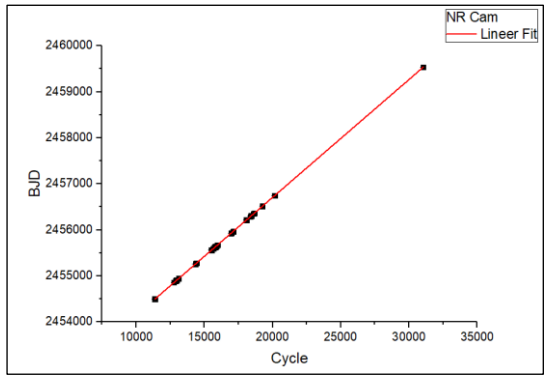

Şekil 5. Tüm minimum zamanlara uygulanan lineer efemeris modeli

Burada, T_0doğruluğundan emin olunan başlangıç minimum zamanı, P_0 sistemin yörünge dönemini, L ise T_0'dan itibaren meydana gelen örtülme sayısını temsil eder [15]. Tüm minimum zamanları ile Denklem 3 kullanılarak NR Cam sisteminin başlangıç minimum zamanı ve yörünge dönemi aşağıdaki gibi bulundu.

$$BJD = BJD\ 2451589.74618272(10) + L \times 0.2558861610(3)$$

Tüm minimum zamanları için elde ettiğimiz yeni başlangıç minimum zamanı ve yörünge dönemi ile sistemin O-C diyagramı Şekil 6'daki gibi elde edildi.

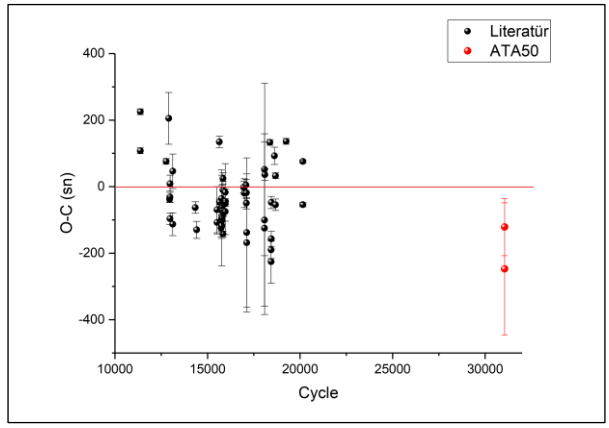

Şekil 6. NR Cam sisteminin O-C diyagramı

4. Tartışma ve Sonuçlar

Bu çalışma kapsamında NSVS2175434, V783 And, ASAS J020753+2034.1 ve NR CAM W Uma tipi dört örten çift yıldız sisteminin fotometrik gözlemleri yapılarak yörünge dönem değişimleri incelendi. İncelenen kaynaklardan NSVS2175434 sisteminin parlaklığı 13.6 kadir ve periyodu ise 0.221 gündür [16]. V783 And sistemi ise 13 Kasım 2013 tarihinde SuperWASP (Super Wide Angle Search for Planets) teleskobu ile keşfedildi ve 0.2090808 gün dönemli EW (W UMa) türü sistem olarak

sınıflandırıldı [17]. Diğer bir sistem olan ASAS J020753+2034.1 ise ASAS (All Sky Automated Survey) ile belirlenmiş olup parlaklığı yaklaşık 12.85 (V) kadirdir [18]. Son olarak NR Cam sistemi, Strohmeier (1958) tarafından başlangıçta 215 Cam olarak adlandırılan yavaş değişen bir yıldız olarak keşfedildi [14, 19]

Bu dört W Uma tipi örten çift yıldız sistemleri ATA50 teleskopu ile gözlemleri yapılarak dokuz yeni örtülme ışık eğrisi elde edildi. Bu ışık eğrileri gauss ve polinom fonksiyonlarının yer aldığı Gauss+Pol fonksiyonu ile fit edilerek dört kaynağa ait minimum zamanları elde edildi (Şekil 1, 2, 3 ve 4). Daha sonra O-C diyagramlarını oluşturabilmek için sistemlere ait literatürdeki minimum zamanları araştırıldı. NR Cam kaynağının dışındaki diğer üç kaynağın literatürde yeterli minimum zamanına sahip olmadığı için O-C diyagramı oluşturulamadı. Ancak, bu çalışma ile literatüre kazandırılan üç kaynağa ait minimum zamanları bundan sonra ki O-C çalışmaları için oldukça önemlidir.

Literatürde yeterli minimum zamanına sahip olan NR Cam için hesapladığımız başlangıç minimum zamanı ve sistemin yörünge dönemi Tavakkoli vd. (2015) tarafından verilenler ile uyumludur. Ancak Şekil 5'de de görüldüğü gibi NR Cam sisteminin O-C diyagramında net bir değişime rastlanamadı. Sonraki süreçte yörünge döneminde değişimin olup olmayacağını daha iyi anlayabilmek için daha uzun dönemli gözlem verilerine ihtiyaç duyulmaktadır

Teşekkür

Bu çalışmada, Atatürk Üniversitesi Astrofizik Araştırma ve Uygulama Merkezi (ATASAM) tarafından işletilen ATA50 teleskobu ve arkasındaki CCD kamera ile elde edilen veriler kullanılmıştır. ATA50 teleskobu Atatürk Üniversitesi (P. No. BAP-2010/40), CCD kamera ise Erciyes Üniversitesi (P. No. FBA-11-3283) Bilimsel Araştırma Projeleri Koordinatörlüğü Birimi (BAP) tarafından finanse edilmiştir. Gerekli verilerin toplanması için gözlem zamanı tahsis eden ATASAM yönetimi ve personeline teşekkür ederiz.

Bu makale, Atatürk Üniversitesi Fen Fakültesi Astronomi ve Uzay Bilimleri Bölümü lisans öğrencilerinin bitirme tezi kapsamında yapılmıştır. Bu kapsamda desteklerini esirgemeyen bölüm Öğretim Üyelerine teşekkür ederiz.

Çıkar Çatışması

Yazarlar herhangi bir çıkar çatışması olmadığını beyan etmektedirler.

Kaynaklar

[1] Binnendijk, L., 1970. The orbital elements of W Ursae Majoris systems. Vistas in Astronomy, 12(1) 217−256
[2] Karttunen, H., Kröger, P., Oja, H., Poutanen, M., Donner, K. J., 2007. Fundamental Astronomy. Springer, 510s, New York
[3] Percy, J. R., 2007. Understanding Variable Stars. Cambridge University Press, 350s, Kanada
[4] Binnendijk, L., 1977. Synthetic light curves for contact binaries. Vistas in Astronomy, 21(4), 359−391

[5] Lee, J. W., Kim, S. L., Kim, C. H., Koch, R. H., Lee, C. U., Kim, H. I., Park, J. H., 2009. The sdB+M Eclipsing System HW Virginis and its Circumbinary Planets. The Astronomical Journal, 137(2), 3181–3190

[6] Gozdziewski, K., Nasiroglu, I., Slowikowska, A., Beuermann, K. et al., 2012. On the HU Aquarii planetary system hypothesis. Monthly Notices of the Royal Astronomical Society, 425(2), 2, 930–949.

[7] Gozdziewski, K., Slowikowska, A., Dimitrov, D., Krzeszowski, K. et al. 2015. The HU Aqr planetary system hypothesis revisited. Monthly Notices of the Royal Astronomical Society, Volume 448(2), 1118–1136

[8] Marsh, T.R., Parsons, S.G., Bours, M.C.P., Littlefair, S.P. et al., 2014. The planets around NN Serpentis: still there. Monthly Notices of the Royal Astronomical Society, 437(1), 475–488

[9] Nasiroglu, I., Gozdziewski, K., Slowikowska, A., Krzeszowski, K., Zejmo, M., Zola, S., Er, H. et al., 2017. Is There a Circumbinary Planet around NSVS 14256825?. The Astronomical Journal, 153(3), 11

[10] Er, H., Özdönmez, A. and Nasiroglu, I, 2021. New observations of the eclipsing binary system NY Vir and its candidate circumbinary planets. Monthly Notices of the Royal Astronomical Society, 507, 809-817

[11] Beuermann, K., Breitenstein, P., Debski, B., Diese, J. et al. 2012a. The quest for companions to post-common envelope binaries. II. NSVS 14256825 and HS0705+6700.Astronomy & Astrophysics, 540(A8), 5

[12] http://simbad.u-strasbg.fr/simbad/sim-fbasic

[13] Eastman, J., Siverd, R., Gaudi, B. S., 2010. Achieving Better Than 1 Minute Accuracy in the Heliocentric and Barycentric Julian Dates. Publications of the Astronomical Society of the Pacific, 122(894), 935

[14] Tavakkoli, F., Hasanzadeh, A., and Poro, A., 2015. The first light curve analysis of eclipsing binary NR Cam. New Astronomy, 37, 64-69

[15] Hilditch, R.W., 2001. An Introduction to Close Binary Stars. Cambridge University Press, 381s, ABD

[16] Kjurkchieva, D., P., et al., 2018. Observations and light curve solutions of three ultrashort-period W Uma binaries. New Astronomy, 62, 41-45

[17] https://www.aavso.org/vsx/index.php?view=detail.top&oid=286477

[18] Pojmanski, G., Pilecki, B., and Szczygiel, D., The All Sky Automated Survey. The Catalog of Variable Stars. V. Declinations 0 deg - 28 deg of the Northern Hemisphere. ArXiv, arXiv:astro-ph/0508017

[19] Strohmeier, W., 1958. kleineveröffentlichungen der Remeis-Sternwarte. Bamberg., No. 23

Atatürk Üniversitesi
Anadolu Fizik ve Astronomi Dergisi
(ISSN: 2791-8718)
Cilt 2, Sayı 1, 43,50

Atatürk University
Journal of Anatolian Physics and Astronomy
(ISSN: 2791-8718)
Volume 2, Issue 1,43 , 50

JAPA

ITO gas sensors for CO_2 and H_2 detection

Sadna Işık[1], Ömer Çoban[2], Cyrus Shafai[1], and Emre Gür*[3]

[1]University of Manitoba, Electric and Computer Engineering, Winnipeg, Canada
[2]Atatürk University, Faculty of Engineering, Department of Electrical Engineering, 25240, Erzurum, Turkey,
[3]Atatürk University, Faculty of Science, Department of Physics, 25240, Erzurum, Turkey

ORCID*[3]: https://orcid.org/0000-0002-3606-2751

Research Type: Research Article

Received: 08.04.2022 Accepted: 03.06.2022

*Corresponding author: emregur@atauni.edu.tr (E. Gür)

Abstract

Thin films with extensive characteristics and surface morphology are very important in designing high performance and reliable gas sensors. Therefore, comprehensive study carried out on ITO transparent conductive oxide resistive based H2 and CO2 gas sensors. As a result, bottom up prototype gas sensor device fabricated and tested in order to understand those properties and behaviors that effects on sensitivity. All the thin film deposited employing RF magnetron sputtering technique investigated by SEM, XRD, EDAX and Absorption methods. Different oxygen partial pressure introduced as a variable to optimize the surface thin film. Those synthesized material properties showed reasonable correlation with the sensitivities and response of ITO devices for reducing H2 and CO2 gases.
Key Words: Gas sensors, CO2 sensor, H2 sensor, RF sputtering, ITO

CCD ve CMOS Sensörlerin Çalışma Prensipleri ve Astronomi Alanındaki Yeri

Özet

Yüksek perfromanslı güvenilir gaz sensörlerinde ince filmlerin detaylı karakteritikle ve yüzey morfolojileri çok önemlidir. Bu nedenle şeffaf iletken oksit İTO direnç tabanlı H2 ve CO2 gaz sensörleri üzerinde kapsamlı bir çalışma yapılmıştır. Sonuç olarak, hassasiyete etki eden özellikleri ve davranışları anlamak için aşağıdan yukarıya prototip gaz sensör cihazı üretilmiş ve test edilmiştir. RF magnetron püskürtme tekniği kullanılarak biriktirilen tüm ince filmler SEM, XRD, EDAX ve Soğurma yöntemleri ile incelenmiştir. İnce filmlerin yüzey yapılarını optimize etmek için, değişken oksijen kısmi basıncı altında filmler büyütülmüştür. Sentezlenen bu

malzemelerin özellikleri, H2 ve CO2 gazlarını indirgemek için ITO tabalı gaz sensörü aygıtlarının duyarlılıkları ve tepkisi ile kabul edilebilir bir korelasyon gösterdi.
Anahtar Kelimeler: gaz sensör, H2 sensör, ITO

1. Introduction

The gas sensors are requisite devices in regular life for detection odorless, hazards, toxic or explosive gases concerning public safety and environmental protection. Consequence of variety of technology and materials has been experimented to invent and explore best suited qualities of materials for improving characteristics of the sensors such as sensitivity, selectivity, and calibration stability, temperature [1,2]. Among those electronic noses, H2 and CO2 sensors started to flourish for their importance in variety of industries, transportation, environmental and health related fields. For instance, high pressure hydrogen gas becoming one of the most important alternative energy known as green energy with zero emission [1]. Thus hydrogen leak detection sensor technology became one of the priority concerns about reliability, safety, and economic reasons [2]. On the other hand, measurement and regulation of CO2 gas is required in indoor spacing, agriculture field and bio-related processes [3]. Even though number of H2 and CO2 sensor exist, those are not sufficient when considering demand, simplicity and the cost perspective.

The indium tin oxide (ITO) wide optical band gap semiconductor thin films as a sensitive layer for gas detection investigated which widely applied as transparent conducting electrodes in flat-panel displays (FPD) [4], solar cells [5], and organic light emitting diodes (OLEDs) [6] due to their process dependency and highly degenerate electrical conductivity [8], high optical transparency [7]. ITO also can be considered as doped from In2O3 materials, known that very common material for gas detection[8]. Furthermore, ITO thin films with careful control of synthesis conditions can be achieved relatively low resistivity while maintaining high transparency that enhance the sensitivity of gas sensors.

Various growth conditions have an effect of increment in the carrier concentrations contributing to the widening of the bandgap, which is known as the Burstein– Moss shift. In addition to the carrier concentration, growth conditions strongly affect the crystallinity, impurity levels and surface roughness of the grown films. In this work, ITO thin film deposited employing RF-magnetron sputtering on soda lime glass substrate that method which characterized by high purity, low substrate temperature, good interfacial adhesion, high thickness uniformity and homogeneity [9]. The effect of O2 partial pressure, on the structural, optical, and sensing properties of the ITO thin film deposited by RF-magnetron sputtering were successfully investigated. Furthermore, resistive based simple concept, low cost, repeatable, mass scale gas sensor device based on ITO thin film sensitive layer gas sensors fabricated. All thin film deposited on interdigitated electrodes (IDE) soda lime glass substrate operated at room temperature without post heat treatment. Moreover, structural and surface characterizations carried out by absorption techniques, x-ray diffraction (XRD) and field emission scanning electron microscope (FESEM). With help of analysis techniques remarkable transmittance and figure of merit observed. Importantly mechanism analysis were undertaken to study the correlation between the sensor performance and the materials structure. The gas-sensing

properties of the thin films were examined exposing the H2 and CO2 gas. The relationships between O2 content and sensor performances were concluded. The influencing characteristics in the evaluation of the thin film also discussed. The gas sensitivity is explained by a change of the band bending on the surface of the metal oxides caused by adsorption of gas molecules. It is expected and proved that these prepared ITO thin films are promising for a H2 and CO2 gases.

2. Experiment

As illustrated in Figure 1, CO2 and H2 ITO sensors were fabricated through microfabrication process based on radio frequency (RF) magnetron sputtering system derived from 14 cm ITO metal target with high purity (ITO - 99.99%, 90% In2O3 and 10% SnO2), in pure Ar and Ar/O2 plasma. Indium tin oxide (ITO) thin films with a thickness of between 500nm-800nm deposited on soda lime glass (SLG) substrate and IDE patterned SLG substrate by reactive magnetron RF sputtering technique. The deposition optimized by changing O2 partial pressure that has impact on crystallographic structure and opto-electrical properties of the films and on sputtering chamber conditions. The partial pressure of the oxygen in the chamber was varied up to 25% of growth pressures.

Standard cleaning procedure (ultrasonic bath of acetone, isopropyl, methanol and de-ionized water for 5 min.) followed to remove contaminants prior to deposition of ITO thin film and samples used in the device. The sensor fabrication was subjected to series of lithography process to fabricate all prototype sensors. As seen in the right side of the Figure 1, the lithography process was started with the photo resist coating by spin coating system under 5000 rpm condition for 50s followed by a soft bake at 110 0C. After exposure of UV light with the mask aligner SUSS Microtech MJB4, developing step was done for 5 min. The lithography process was finished by the hard bake at 120 0C for 2 min. All the sensors sensitivity measurement obtained by non-commercially available gas measuring system.

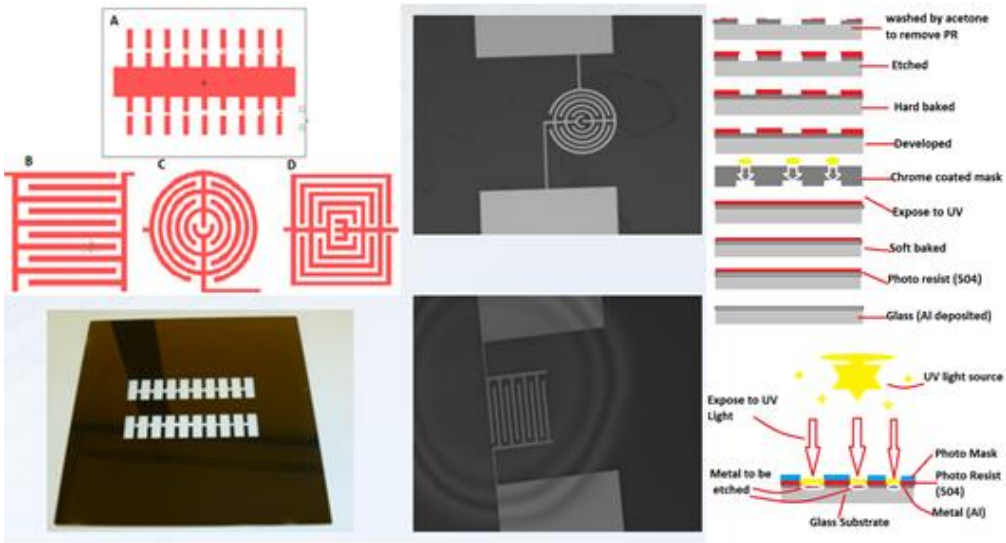

Figure 1. ITO thin film growth and sensor fabrication process.

The morphology characterization of the samples grown was performed with (FESEM) with Zeiss Sigma 300. The elemental analysis also was conducted with energy dispersive x-ray (EDX) detector attached to the FESEM system. The XRD measurements were made θ-2θ condition between 10-90-degree PANalytical Empyrean XRD system.

3. Results and Discussion

From EDX composition analysis in Figure 2 a and the results in tabulated in Figure 2 b show that ITO film grown with ITO target deposited with pure Ar plasma with no oxygen gas contain zero Sn. This could be the result of that indium was formally evaporated because of its lower boiling point than Sn [10]. On the other hand, as the oxygen is included during the growth, the Sn composition appears in the EDX measurements (figures not shown). The Sn amount in ITO thin film is an important factor to

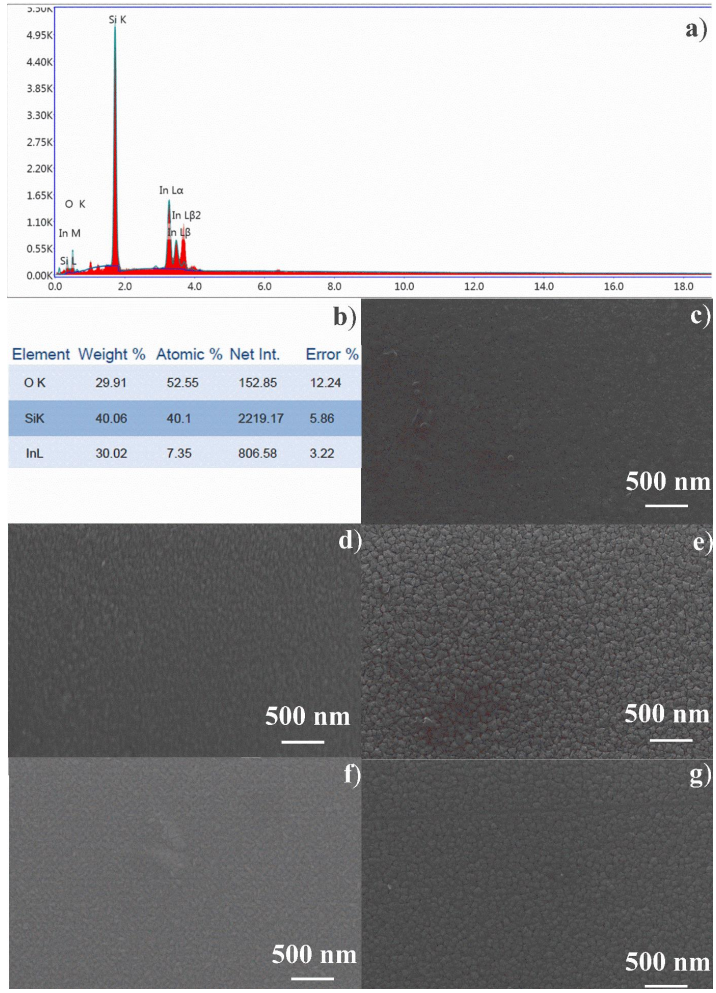

Figure 2. a) EDX data for the ITO grown under no oxygen pressure b) EDX element analysis c)-g) FESEM images of the ITO films of different oxygen partial pressure percentages to the total growth pressure 0%, 2.7%, 11.7%, 13.5%, 16.3%, respectively.

decrease the resistance of prepared ITO film [11], this no Sn contain sensor has shown the highest sensitivity. Figure 2 c-g have shown the FESEM images of the ITO thin films grown under different oxygen partial pressure percentages, 0%, 2.7%, 11.7%, 13.5%, 16.3%, respectively. It is shown that as the oxygen partial pressure percentage increases, the grain sizes observed in the FESEM images increase which is maximum for the 11.7% grown ITO film.

Figure 3 shows the XRD pattern of the sputtered ITO grains. The dominant peaks are indexed as (400) and (441) crystal faces of ITO which confirmed that the gains are polycrystalline. Increasing with the O2 content, the peak intensities belong to the ITO planes are increased as seen in the figure. Table 1 shows the calculated D values from the measured of the XRD data. The D values varies between 27 nm- 77 nm as seen in the table.

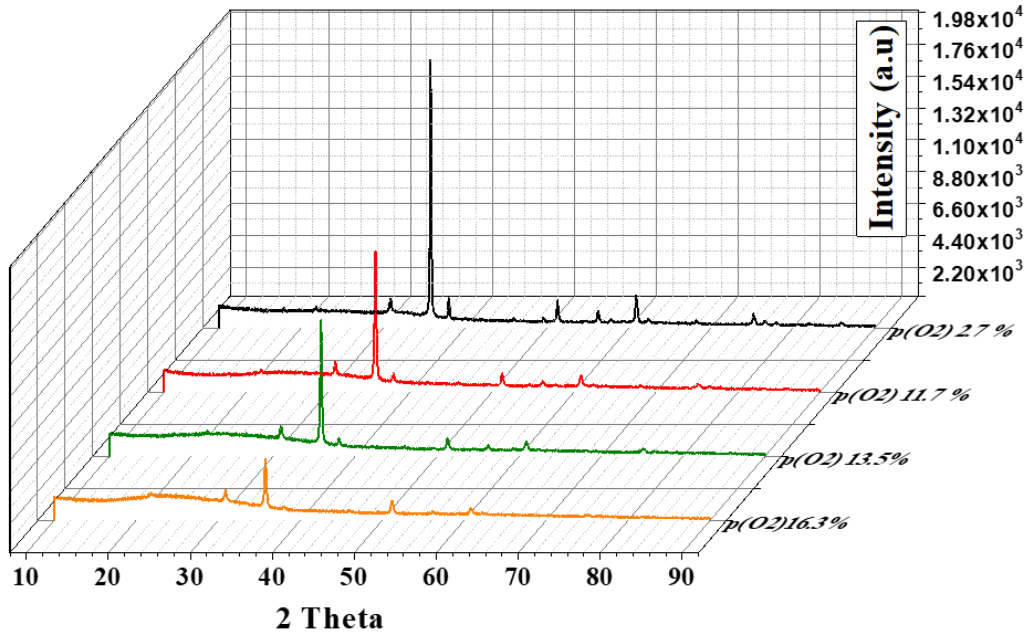

Figure 3. XRD figure of ITO films grown different O2 partial pressures

Table 1. Detail analysis of the XRD measurements

O_2%	Thickness (nm)	2θ (400)	I% (400)	FWHM (400)	D (nm)	2θ (441)	I% (441)	FWHM (441)
0	333	-	-	-	-	-	-	-
2.7	983	35.8	100	0.13	62.8	51.3	8.61	0.17
11.7	250	35.8	100	0.30	27.8	51.2	82.6	0.20
13.5	335	35.8	83.9	0.19	56.5	51.2	100	0.16
16.3	825	35.7	100	0.11	76.6	51.1	15.6	0.17
25	402	35.8	100	0.21	39.4	51.2	29.4	0.23

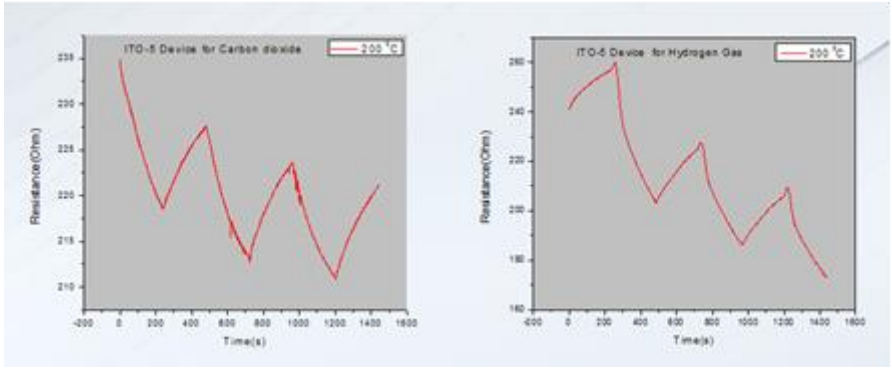

Figure 4. CO2 and H2 responses of the ITO sensor grown under 0% oxygen pressure.

Figure 4 shows a representative dynamic curve of the ITO sensor grown with no oxygen gas in the chamber. The concentration of CO_2 and H_2 for this test was 400 sccm. The optimal temperature to detect CO_2 and H_2 gases is at 200 ^{0}C which is plotted in Figure 4. The optimal working temperature is relatively lower than that of ITO thin film sensor which reported in other studies [7]. The resistance change, ΔR, of the sensors is monitored during sequential or periodic exposures to H_2 or CO_2. $\Delta R/R_0$ (sensitivity) is defined as the percent resistance change upon exposure to a gas with a fixed concentration of hydrogen and is calculated according to $\Delta R/R_0 = (R - R_0)/R_0$ where R_0 is the resistance of the sensor exposed to N_2 air and R is the maximum resistance after exposure to a gas containing hydrogen. Consequently, decreasing of the work function is beneficial to the flow of more electrons, resulted in decreasing of the resistance [12].

Good sensitivity (22%) of ITO sensor that contains no oxygen flow included during the growth could be related to the surface to volume ratio of nano-grains of the thin film. Table 2 and 3 have shown the responsivity, response and recovery time for some of the ITO sensors produced in the study. Recovery times for the CO_2 sensors are long. The reason for longer recovery time might be attributed that it took longer time for CO_2 desorbing from the nano-gains. A detail investigation expecting to carry out in future studies to find CO_2 adsorbing and desorbing by thin film. The fact that ITO nano grains have very large surface to-volume ratio which means a significant fraction of the atoms of ITO are surface atoms that can participate in surface reactions. This feature would contribute the resistance change of the ITO nano-grains, thus enhance the response the sensor and optimal working temperature. Another reason was related to the nature of the ITO surface, which was easy to react with H_2 because Sn doped material reported good sensitivity for H_2. Table 2 and Table 3 have shown the performances of the gas sensors characteristics.

Table 2. Responsivity, Response Time, Recovery time for H_2 at 200 ^{0}C

Responsivity ((R-R0)/R0)*100			Response Time(S) (1-1/e)			Recovery time(s) (1/e)		
2.7%	25%	%0	2.7%	25%	%0	2.7%	25%	%0
10.9	9.8	22	32.8	23.6	92.3	36.4	4.4	24.2

Table 3. Responsivity, Response Time, Recovery time for CO_2 at 200 ^{0}C

Responsivity ((R-R0)/R0)*100			Response Time(S) (1-1/e)			Recovery time(s) (1/e)		
2.7%	25%	%0	2.7%	25%	%0	2.7%	25%	%0
9.2	6.0	4.1	39.8	10.5	68.1	62.1	28.7	105.8

Semiconductor gas sensors are based on the conductivity changes of the semiconductor materials upon interaction with the target gas molecules. When the H_2 molecules were absorbed on the surface of the ITO nano-grains, electron transfer occurs between ITO and target gases. When the temperature was increased, the molecules were easier to react and be absorbed on the adsorption sties. However, desorption process existed at the same time. When the temperature was too high, the desorption process would become dominating which lowered the absorption of the gas. Consequently, there was an optimum working temperature for ITO nano-grain based sensor. A systematic investigation needed to prove further for CO_2. Besides the sensor response other parameters such as selectivity, response time and stability, are also very important. The testing for these parameters is in progress [13].

The dependence of the resistivity on the oxygen partial pressure is a well-known experimental result and is explained on the basis of oxygen deficiency in the film (each oxygen vacancy gives rise to two conduction electrons). Increasing oxygen content of the films by increasing the partial pressure of oxygen during the growth the samples in air or oxygen should decrease the oxygen vacancies leading to less conductive films. However, a minimum in the resistivity of the ITO thin films deposited on glass substrates is reported between 15 and 20% of oxygen partial pressure by a few investigators indicating an improvement in the crystallinity of the films (mobility of the carriers is dependent on crystallinity) [14].

4. Conclusion

ITO thin film has been successfully prepared by RF sputtering technique with the goals of improving sensitivity, simplicity and with RT temperature and without post heat treatment by enhancing performance of thin film controlling O_2 ratio for in H_2 and CO_2 sensing. The innovative sensing platforms demonstrated excellent sensitivity, response and recovery time. Device dependent sensitivities tested for range of operating temperature between of 30 °C – 200 °C. The distinct surface morphology and properties of ITO thin film with grain sizes play a key role improving sensitivity of

these sensors. The present result evidently proves that the methodology that applied to design ITO sensors could be one of the most promising TCO oxide-based gas sensors.

5. Acknowledgment

The authors thank the solid-state physics laboratory, Ataturk University, nano fabrication laboratory, university of Manitoba, physics laboratory, Erzincan University for supporting this research. This work gas measurement system was financially supported by Atatürk university Bap project number 2015/93 which is gratefully acknowledged.

Conflicts of interest

The authors declare that there are no potential conflicts of interest relevant to this article.

References

[1] Ying-Ting Wang, Wha-Tzong Whang, and Chun-Hua Chen Hollow V2O5 Nanoassemblies for High-Performance Room-Temperature Hydrogen Sensors DOI: 10.1021/am509182s ACS Appl. Mater. Interfaces 2015, 7, 8480−8487

[2] Gary W. Hunter, Philip G. Neudeck, G.D. Jefferson, and G.C. Madzsar the development of hydrogen sensor technology at nasa lewis research center Fourth An_nual Space System Health Management Technology Conference sponsored by the American Institute of Aeronautics an dA=stronautic Cincinnati, Ohio, November 17-18, 1992

[3] Kenji Obata, Shizuko Kumazawa, Shigenori Matsushima, Kengo Shimano, Noboru Yamazo NASICON-based potentiometric CO2 sensor combined with new materials operative at room temperature, Sensors and Actuators B 108 (2005) 352–358

[4] H.S. Uhm, B.H. Hong, P.Y. Oh, E.H. Choi, Properties of excited xenon atoms in a plasma display panel, Thin Solid Films 517 (2009) 4023–4026.

[5] S. Gunes, N.S. Sariciftci, Hybrid solar cells, Inorg. Chim. Acta 361 (2008) 581–588.

[6] Y.J. Lee, J.H. Kim, J.N. Jang, I.H. Yang, S.N. Kwon, M.P. Hong, D.C. Kim, K.S. Oh, S.J. Yoo, B.J. Lee, W.G. Jang, Development of inverted OLED with top ITO anode by plasma damage-free sputtering, Thin Solid Films 517 (2009) 4019– 4022.

[7] Z. Jiao, M.H. Wu, J.Z. Gu, X.L. Sun, The gas sensing characteristics of ITO thin film prepared by sol–gel method, Sens. Actuators B 94 (2003) 216–221.

[8] T. Wagner, T. Sauerwald, C.-D. Kohl, T. Waitz, C. Weidmann, M. Tiemann, Gas sensor based on ordered mesoporous In2O3, Thin Solid Films 517 (2009)6170–6175.

[9] H.S. Al-Salman, M.J. Abdullah Hydrogen gas sensing based on ZnO nanostructure prepared by RF-sputtering on quartz and PET substrates Sensors and Actuators B 181 (2013) 259– 266

[10] Three electrodes gas sensor based on ITO thin film Sang-Mun Leea, Yun-Su Leea, Chang-Hyun Shima, Nak-Jin Choia, Byung-Su Jooa,Kap-Duk Songa, Jeung-Soo Huhb, Duk-Dong Leea,* Sensors and Actuators B 93 (2003) 31–35

[11] The gas sensing characteristics of ITO thin film prepared by sol–gel method Zheng Jiao∗, Minghong Wu, Jianzhong Gu, Xilian Sun Sensors and Actuators B 94 (2003) 216–221

[12] Low temperature high sensor response nano gas sensor using ITO nanofibers Shiyou Xu, Yong Shi∗ Sensors and Actuators B 143 (2009) 71–75

[13] Electrical, optical and structural characteristics of indium-tin-oxide thin films deposited on glass and polymer substrates A.K. Kulkarnia,*, K.H. Schulzb, T.-S. Lima, M. Khanb Thin Solid Films 308–309 (1997) 1–7

[14] Flower-like Palladium Nanoclusters Decorated Graphene Electrodes for Ultrasensitive and Flexible Hydrogen Gas Sensing Dong Hoon Shin, Jun Seop Lee, Jaemoon Jun, Ji Hyun An, Sung Gun Kim, Kyung Hee Cho & Jyongsik Jang Scientific Reports | 5:12294 | DOI: 10.1038/srep12294

Atatürk Üniversitesi
Anadolu Fizik ve Astronomi Dergisi
(ISSN: 2791-8718)
Cilt 2, Sayı 1, 51-59
Atatürk University
Journal of Anatolian Physics and Astronomy
(ISSN: 2791-8718)
Volume 2, Issue 1, 51-59

JAPA

Working Principles of CCD and CMOS Sensors and Their Place in Astronomy

[*1]Ahmet Polatoğlu, [1]İmam Can Özkesen

[*1]Atatürk University, Faculty of Sciences, Department of Astronomy and Space Science, 25240 Erzurum, Turkey.

ORCID[*1]: https://orcid.org/0000-0002-6562-8566
ORCID[1]: https://orcid.org/0000-0002-3454-5442

Research Type: Review Article

Received: 17.03.2022, Accepted: 22.04.2022

*Corresponding author: ahmet.polatoglu@atauni.edu.tr (A. Polatoğlu)

Abstract

In this article, information about the properties, working principles and recent developments of CCD and CMOS sensors used in astronomy are given. Until the development of camera technology, sky observations were made using photographic plates in telescopes. With the development of CCD sensors in the 1960s, photographic plates were replaced by powerful cameras with CCD and CMOS sensors. Even today, all observations made in the optical field are made with the data taken by placing these cameras in the ocular part of the telescope. It is of great importance to understand the sensor technology in order to understand the observation techniques. This article has been prepared to fill this gap.
Key Words: Astronomy, Telescope, Sensor, CCD, CMOS.

CCD ve CMOS Sensörlerin Çalışma Prensipleri ve Astronomi Alanındaki Yeri

Özet

Kamera teknolojisinin gelişmesine kadar, teleskoplarda fotoğraf plakaları kullanılarak gökyüzü gözlemleri yapılmıştır. 1960'larda CCD sensörlerinin geliştirilmesiyle, fotoğraf plakalarının yerini CCD ve CMOS sensörlü güçlü kameralar aldı. Bugün bile optik alanda yapılan tüm gözlemler, bu kameraların teleskoplara monte edilerek alınan verilerle yapılmaktadır. Gözlem tekniklerini anlamak için sensör teknolojisini anlamak büyük önem taşımaktadır. Bu makalede CCD ve CMOS sensörlerin özellikleri, çalışma prensipleri ve son gelişmeler hakkında bilgi verilmiş ve sensör teknolojisinin astronomide kullanımı incelenmiştir.
Anahtar Kelimeler: Astronomi, Teleskop, Sensör, CCD, CMOS.

1. Introduction

Photosensitive digital cells are called sensors or optical sensors. CCD and CMOS sensor technology are used today in camera systems, cameras of mobile phones, digital cameras and many systems that are sensitive to image creation. As a result of the demand for these systems, sensor technology is gaining momentum day by day.

The sensors convert the incoming optical image into electronic signals. They consist of light-sensitive cells called photodiodes on sensors. Photodiodes receive light and convert photons into electrical signals. The resolution/pixel of the sensor is proportional to the number of photodiodes. For example, 10 megapixels means 10 million photodiodes. The higher the resolution, the higher the detail quality. If the sensor is produced in small sizes, the photodiodes will be smaller and accordingly less light will be received. Thus, it is understood that sensors with high pixels do not always have high quality. Light sensitivity needs to be increased in order to both use small photodiodes and improve image quality [1].

It is important in terms of image quality that the sensors used in astronomy are produced in large sizes. However, due to the widespread use of mobile products and being more commercial/economical products, small-sized sensors are produced more [2]. Especially silicon sensor technology is used in the field of astronomy. Due to the need for large focal planes in astronomy, large CCD sets have been produced. Newly produced CCD and CMOS sensors are designed with low noise and high measurement accuracy. This feature is also important for obtaining accurate data in astronomical observations [1,3].

2. Material and Methods

2.1. Fundamentals of Sensor Technology

Sensors are devices or subsystems that detect events/information in their environment and send them to other electronic devices (processors). The sensors are used compactly with other electronic devices. In addition to numerous applications, it is also used in everyday objects such as lamps that darken or brighten when touched. With the development of micro-devices and simple-to-use microcontrollers, the use of sensors has moved beyond the very general pressure, humidity or flow measurements. Sensors are generally designed to have little effect on what is being measured. Reducing the size of the sensor often makes it better and provides convenience. Technological developments have opened the door to the production of more sensors at microscopic scale with micro sensors using MEMS technology. Oftentimes, a micro-sensor provides a very fast and short measurement time and higher precision results compared to large systems. Today, the demand for fast, economical and reliable information has increased. Thus, the importance of disposable sensors has increased recently. Using them, important analytical data can be easily obtained by anyone without any problems [1].

There are two basic types of sensors used in almost all digital camera/measurement systems. One of them is CCD (Charge Coupled Device) sensor and the other is CMOS (Complementary Metal Oxide Semiconductor) sensor. CMOS sensors are divided into two main groups as passive pixel sensors and

active pixel sensors. There is also a type of sensor that can capture three colors in a single pixel [4]. We will discuss on CCD and CMOS in this article.

2.2. CCD (Charge Coupled Device)

CCD (Charge Coupled Device) sensors, which were discovered by Willard Boyle and George Smith in 1969, have been developed with the advancement of technology and have come to the present day. The working logic of the CCD sensor is to capture the photons coming from the light source. These captured photons form photoelectrons. The resulting photoelectrons are collected in cells called photocells. These electrons formed in the cells are counted and stored together with their coordinates [4].

There are versions of CCD sensors produced and put into use in different ways. One of them, One Chip-One Shot technology, has three basic color-sensitive filters, RGB (Red-Green-Blue) on the sensor. In this way, basic color separation is done on the CCD. CCDs produced by this method are mostly used in entry-level products. It has relatively low costs. In addition to the Two-Chip method RGB filter, there is also a second sensor for brightness. Another method is One Chip-Three Shot technology. In this, after the light falling on the sensor is divided into three parts, RGB, it is exposed with a special filter. Regardless of the technology, CCD sensors are expensive to manufacture, require more energy than other sensors, and require a large area for use. Therefore, CCD sensors are not generally preferred in mobile phones. CCD sensors are more preferred in fields such as special astronomy, as they give relatively higher quality and clear images [5].

2.2.1. Working Principle of CCD

CCDs are based on Metal Oxide Semiconductor (MOS) capacitors technology. Embedded channel capacitors are used for manufacturing. A thin n-type embedded channel is formed by ion doping on the surface of a p-type substrate. A silicon dioxide insulator layer is formed over the n-region and metal or heavily doped polycrystalline silicon gates are placed on top of the CVD (chemical vapor deposition) insulated SiO_2 to fill the capacitor. The main material of CCDs is mostly silicon semiconductors. These sensors are extremely sensitive to light. Capturing photons from the light source, a CCD cell performs four tasks: It takes the charge from the cell above the layer, holds the charge for a while, transfers this charge to the cell below the layer, and produces its own energy. It charges by reacting to external factors such as light [1].

Rays from the light source form photoelectrons. The resulting photoelectrons are collected in the cells in photocells. These electrons formed in cells are counted and stored together with their coordinates. CCD sensors, whose raw material is usually silicon semiconductors, have a light sensitive structure. They convert light into electronic signals and are sent to image processors for processing with this sensitivity. The signals processed on the image processor are converted into digital signals and stored on memory cards [1][4].

The speed, sensitivity, resolution, and cost of a CCD sensor affect its performance. Which CCD type to choose depends on the areas where the devices will be used. Frame transfer structure is used in

astronomy because maximum light must be captured. However, the most used in cameras is the interline transfer structure. The three structures used to apply the value read from the CCD array can be described as follows:

i. Full Frame: The entire CCD array acts as the active area. Charges pass through vertical CCDs in parallel and are then removed in series from horizontal CCDs, using a shutter mechanism to block light from reaching the elements. This process takes a lot of time.

ii. Frame Transfer: Half of the adjacent array area is used for exposure and the remaining half is opaque. Loads are transferred from the active region to the opaque region in a short time and are read from there. This operation is faster than full frame reading. However, it has a disadvantage that it uses twice the silicon area.

iii. Interline Transfer: Each pixel has an active area and an adjacent opaque area. Charges are quickly transferred from the photosensitive photodiode to the adjacent vertical CCD unit. There is also the disadvantage of increasing silicon area here. However, with modern developments, it is possible to increase the quantum efficiency of the array by using micro lenses that direct the light away from the opaque regions [7]

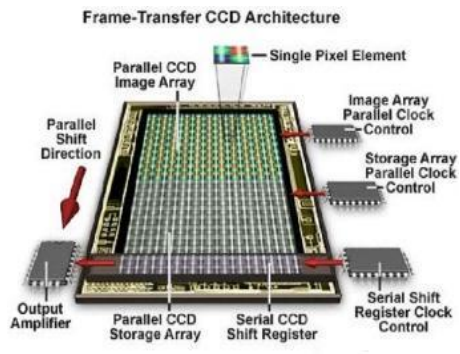

Figure 1. Frame Transfer CCD Architecture [6].

The sensitivity of a CCD device is usually a function of its operating temperature. As the temperature increases, the leakage light-free current also increases, thus decreasing the sensitivity. In devices with a CCD sensor, Signal Noise Ratio (SNR) degradation may occur due to photon noise, readout noise, or a combination of these. CCD arrays are only sensitive to density, not color. Filters are used to obtain color images. Color images can be obtained using a Bayer filter or a 3CCD and dichroic beam splitting prism [8].

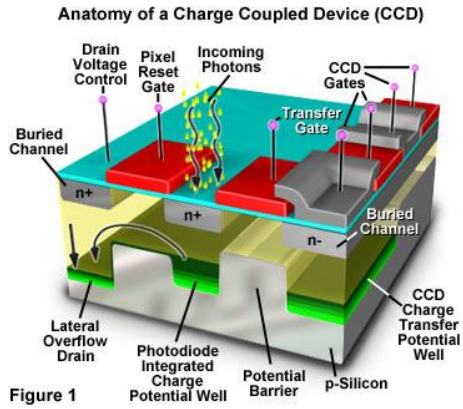

Figure 2. Anatomy of a CCD [6].

2.3. CMOS (Complementary Metal Oxide Semiconductor)

CMOS sensors were discovered by Frank Wanlass in 1963. Like CCDs, they convert light into electronic signals. These sensors consist of hundreds of transistors. Each pixel is generated by a separate transistor. CMOS sensors are widely used. The reason for this is that they have been widely used in devices other than cameras for years and show a continuous development [10],

With this widespread use, CMOS sensors, which can be produced at affordable prices, are often preferred especially in entry-level digital cameras. Especially small floor coverings are one of the most important reasons for this. It is a product frequently encountered in mobile phones, tablets, compact machines and DSLR devices. In addition, factors such as low energy need and not taking up much space play an important role in the preference of these sensors [10,11].

2.3.1. Working Principle of CMOS

CMOS sensors, just like CCD sensors, work according to the photoelectric effect system to convert light into electricity. All CCDs and CMOS sensors perform the same basic tasks: charge generation and collection (light to charge conversion), measurement and conversion to voltage or current, finally signal output.

CCD sensors move the photographic charge from pixel to pixel and convert it to voltage at an output node, as shown in the diagram below; CMOS imagers instantly convert the charge inside each pixel to voltage. Modern CMOS sensors also contain an amplifier for each pixel. After amplification, the voltage output of the pixel is transferred over a micro wire at the output of the chip [11].

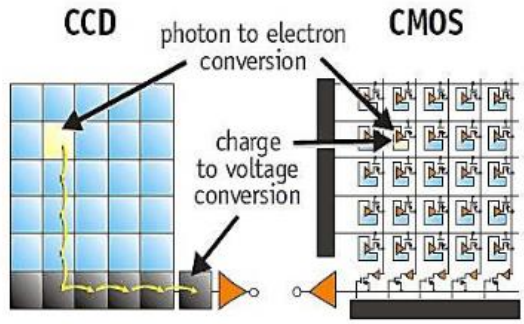

Figure 3. Working differences of CMOS and CCD [11].

2.4. Differnces Between CCD and CMOS

Since CMOS sensors do not take up much space, they are preferred especially in small devices (such as mobile phones, tablets). CMOS sensors can operate with less energy. This means longer battery life. Because CMOS sensor technology is used in many devices, it is inexpensive and easy to manufacture.

CCD sensors generally operate with much lower noise than CMOS sensors. The light sensitivity of CCDs is much higher than that of the CMOS sensor. Therefore, although CMOS gives successful results in bright environments, they give worse results in low light conditions than CCD sensors. CCD sensors produce low noise and high quality images. However, CMOS sensors catch up with the technology and approach CCD technology in terms of quality [12].

3. The Place of CCD and CMOS Sensors in Astronomy

Image quality and low noise are very important in astronomy, as small arcsecond fields are precisely observed. The sensors that meet these conditions have always been CCDs. Although CMOS sensors have been used in astronomy in recent years, CCD use is older and more common.

The use of CCD cameras in astronomy is one of the best detectors we have with current technology, although the CCD chip is not an optically ideal detector. Therefore, it is a detector mostly used in telescopes. External factors such as sensor readout noise, thermal noises, and cosmic rays can alter pixels in the CCD array. So to counter such effects, astronomers take several exposures with the CCD shutter closed and open so that the CCD-acquired images can be analyzed. The average of images (Bias) taken with the shutter closed is required to reduce noise. After the Dark Frame average image is taken, it is subtracted from the light shutter image to clear dark current and other structural defects (dead pixels, hot pixels, etc.) in the CCD. For these processes, images (Bias, Dark, Flat) specific to each CCD are calibrated [12].

3.1. Historical Process and Importance

From the 1900s to the present, there have been great developments in astronomical instruments with telescopes. Telescopes with larger mirror diameters have been produced. Since there are no CCD detectors to record the observation data, photographic images are obtained by using photographic plates (glasses coated with silver halide) placed on the focal plane of the telescope. In addition, the glass wedge placed in the focal plane of the Telescope is adjusted until the intensity of the star is equal to the light intensity of a preselected standard star, and the images taken are calibrated by comparing this glass wedge, and in photographic photometry the brighter the star image on a plate, the larger the star size. Some instruments such as micrometers and thermocouples are used with these photographic plates. In addition, the blink microscopes used for comparison were used to distinguish the differences in the plates by rapidly rotating the plates taken at different times. Although CCDs came into our lives in the 1970s, these methods were used until the end of the 1900s and CCDs replaced photographic plates in astronomy [13].

CCDs were first produced at Bell Laboratories in the 1970s. The first CCD 1969 Willard Boyle and George Smith single array 8 pixel detector. Later, in 1973, the Jet Propulsion Laboratory (JPL), NASA and TI jointly started a large-area CCD development program for Astronomy. The first commercial CCD device was produced by Fairchild in 1974. In 1974, the Moon was imaged using an 8 inch Telescope with a Fairchild CCD (100x100 pixels), and this is the first astronomical CCD image. Among the earliest astronomical applications of a CCD for ground observation were made at the University of Arizona in 1976 (Smith 1976). The first CCD-based reconnaissance satellite, KH-11 KENNAN, was launched in 1976. CCD development continued over the years, and in 1979 Radio Corporation of America (RCA) developed a liquid nitrogen-cooled CCD system [14].

Continuing developments from the 1980s to the present have led to devices with over 100 million pixels, read noise as low as an electron, quantum efficiency close to 100%, and useful sensitivity close to X-rays to IR. While CCDs have fallen out of favor with CMOS imagers for commercial imaging applications, they are still cutting-edge sensors for astronomical imaging due to their size, efficiency and low noise. Over the years, scientists who make astronomical instruments have developed CCDs specific to their areas of interest [1,14].

In 1983, CCDs began to replace photographic plates in astronomical telescopes. Kodak produced CCD-based professional cameras until affordable, high-resolution cameras began to hit the market in 1995 [1].

3.2. Basic Definitions

There are special requirements for astronomical imaging, astronomers have often made special CCD sensors for their own observing needs. These special requirements are:
Pixel Size: Larger than normal pixels are used in astronomy due to sensors, large full well capacity and dynamic range.
Dark Current: Exposures taken with the CCD's diaphragm closed. The electron flow resulting from the heating of the CCD and electronic parts is called black current. The exposure time for Dark is given

as much as the exposure time of the object to be observed. eg. If we are going to observe the Polaris star with exposures of 20 seconds, images are taken with an exposure time of 20 seconds for the dark.

Quantum Efficiency: It is the ratio of the number of photons measured to the number of all incoming photons. If this value is 1, it means that all incoming photons are captured by the detector, and there is no such perfect instrument. An instrument with a quantum efficiency of 90% is considered sensitive.

Bias: It is the exposure taken in zero seconds while the aperture is closed. Returns the electronic noise value in the CCD [12]. Raw Biased Frames are created with zero light to the camera. Science frames are created that take zero-second exposures (shortest exposure) in the same grouping mode (1x1, 2x2). After creating a Master Bias, it can be used until the ambient temperature is too high to regulate the CCD temperature anymore or a change is made to the electronic path of the system.

Dark: The thermal movements of electrons within the chip produce signals gradually, proportional to the exposure time, not because they are exposed to optical light, but because these thermal electrons have a chance to accumulate in each pixel over time. The Dark Frame is made to measure the "dark current" or thermal signal in the CCD chip so that it can be extracted from the data images.

Flat: Not every pixel in the CCD has the same sensitivity. The middle pixels are brighter and the edges are dimmer. These are images taken to correct for different distribution. The exposure time is given as half the saturation level of the pixels. In which filter the object to be observed will be observed, flat is taken in the same filter [12].

4. New Developments

CCD and CMOS sensors have made great advances in recent years. Low noise ratio, high resolution and quality images are provided. CMOS sensors, on the other hand, have caught up with CCD sensors at a better viewing point, although they are made in smaller sizes.

Thinned CMOS sensors have been produced for use in astronomy. Examples of these are TAOS-II CIS113 sensor, NGSD/LGSD CIS112 sensor, CIS115 sensors. For large space programs, sensor technologies such as GAIA CCD91, Euclid CCD273, Plato CCD270, Rosetta have been developed. Studies are also underway on EMCCD and Red Sensitive CCDs [2, 16].

5. Conclusion

What makes a digital camera digital is the image sensor in the camera. That is, an image sensor converts the light captured by the camera's lens into a digital signal. This digitized light is processed and stored in the camera's memory as a digital file that you can view on the computer later. Next to the lens, the image sensor is the key element that ensures quality video. There are two main types of camera image sensors: CCD and CMOS. Both types of image sensor technologies contain hundreds of thousands or even millions of pixels. We can think of a pixel as a small bucket that captures light and converts it into an electrical signal. CCD and CMOS sensors have different advantages, but technology is evolving rapidly and the situation is constantly changing. Therefore, the best strategy for a camera manufacturer is to constantly evaluate and test the sensors for each camera. The field of astronomy

is also an area that can no longer progress without sensor technology. With each passing day, we will see that more powerful sensors are produced.

Conflicts of Interest

The authors declare that there are no potential conflicts of interest relevant to this article.

References

[1] Gourab Sen Gupta, (2008). Smart sensors and sensing technology. 1st ed. Springer.
[2] Jorden P.R., Jordan D., Jerram P.A., Pratlong J., Swindells, I. (2014). e2v new CCD and CMOS technology developments for astronomical sensors. High Energy, Optical, and Infrared Detectors for Astronomy VI, ed. by Andrew D. Holland, James Beletic, 9154(91540).
[3] Büttgen, B. (2005).. CCD/CMOS Lock-In Pixel for Range Imaging: Challenges, Limitations and State-of-the-Art. Researchgate.
[4] Litwiller D. (2001). CCD vs CMOS: Facts and Fiction.
[5] CCD ve CMOS nedir? [Internet]. 2022 [25 February 2022]. Access Link: https://birkarefotograf.com/cmos-ve-ccd-nedir/
[6] Hamamatsu [Internet]. 2022 [12 March 2022]. Access Link: https://hamamatsu.magnet.fsu.edu/articles/ccdanatomy.html
[7] Astro [Internet]. 2022 [05 February 2022]. Access Link: https://www.astro.rug.nl/~ndouglas/teaching/JAFFE/reduce.htm
[8] Aavso [Internet]. 2022 [2 March 2022]. Access Link: https://www.aavso.org/sites/default/files/publications_files/ccd_photometry_guide/CCDPhotometryGuide.pdf
[9] CCD nedir [Internet]. 2022 [1 January 2022]. Access Link: https://www.elektrikport.com/makale-detay/ccd-sensor-nedir/21967#ad-image-1
[10] Lesser, M. A Summary of Charge-Coupled Devices for Astronomy, Publications of the Astronomical Society of the Pacific, 2015; (127)-957.
[11] CMOS Image Sensors, Moazalhosny [Internet] 2017. Access Link: https://www.researchgate.net/publication/316986687_basic_description_of_CMOS_camera_sensor_and_color_precnible.
[12] Astrophotography [Internet]. 2022 [3 January 2022]. Access Link: https://practicalastrophotography.com/a-brief-guide-to-calibration-frames/.
[13] Andor [Internet]. 2021 [25 December 2021]. Access Link: https://andor.oxinst.com/learning/view/article/ccd-sensor-architectures.
[14] Observational Astronomy [Internet]. 2021 [24 February 2021]. Access Link: https://en.wikipedia.org/wiki/Observational_astronomy.
[15] Petrov B. [Internet]. 2021 [16 December 2021]. Access Link: https://www.astro.bas.bg/~petrov/galaxies_files/astroinst.html.
[16] Jorden P.R., Jordan D., Jerram P.A., Pratlong J., Swindells I. (2016). e2v new CCD and CMOS sensors and systems designed for astronomical applications. High Energy, 900-915.